

ANKARA YILDIRIM BEYAZIT UNIVERSITY

GRADUATE SCHOOL OF NATURAL AND APPLIED SCIENCES



**CHARACTERIZATION OF NUCLEAR FUEL ROD CLADDING
ZIRCONIUM ALLOYS**

M.Sc. Thesis by

Semih AĞCA

Department of Material Engineering

June, 2017

ANKARA

**CHARACTERIZATION OF NUCLEAR FUEL ROD
CLADDING ZIRCONIUM ALLOYS**

A Thesis Submitted to

The Graduate School of Natural and Applied Sciences of

Ankara Yıldırım Beyazıt University

**In Partial Fulfillment of the Requirements for the Degree of Master of Science
in Material Engineering, Department of Material Engineering**

by

Semih AĞCA

June, 2017

ANKARA

M.Sc. THESIS EXAMINATION RESULT FORM

We have read the thesis entitled “**CHARACTERIZATION OF NUCLEAR FUEL ROD CLADDING ZIRCONIUM ALLOYS**” completed by **SEMİH AĞCA** under the supervision of **PROF. DR. GÜVEN ÇANKAYA** and we certify that in our opinion it is fully adequate, in scope and in quality, as a thesis for the degree of Master of Science.

Prof. Dr. Güven ÇANKAYA

Supervisor

Prof. Dr. Fahrettin GÖKTAŞ

Jury Member

Prof. Dr. Mustafa ÖZDEMİR

Jury Member

Prof. Dr. Fatih V. ÇELEBİ

Director

Graduate School of Natural and Applied Sciences

ETHICAL DECLARATION

I hereby declare that, in this thesis which has been prepared in accordance with the Thesis Writing Manual of Graduate School of Natural and Applied Sciences,

- All data, information and documents are obtained in the framework of academic and ethical rules,
- All information, documents and assessments are presented in accordance with scientific ethics and morals,
- All the materials that have been utilized are fully cited and referenced,
- No change has been made on the utilized materials,
- All the works presented are original,

and in any contrary case of above statements, I accept to renounce all my legal rights.

ACKNOWLEDGMENTS

First I would like to thank Prof. Dr. Güven ÇANKAYA for his scientific and humanitarian support. His experience and advices helped me while writing this thesis.

I am grateful to Prof. Dr. Fahrettin GÖKTAŞ and Prof. Dr. Mustafa ÖZDEMİR for their valuable contributions in my thesis defense examination.

I also would like to thank Assist. Prof. Dr. Metehan ERDOĞAN and Res. Assist. Mahmut EROL for their contributions in heat treatment process.

I am also grateful to Assoc. Prof. Dr. Çağrı ÇIRAK, Res. Assist. Dr. Fikret YILMAZ, Bayram BAYAR, Abdülaziz GÜNEŞ and Harun ASLANER for their help in experimental studies.

Finally, I would also express my gratitude to my family. This would not have been possible without my mother's prays. My wife Fatma Nur and my daughter Hatice helped me in every step of my studies.

2017, 1 June

Semih AĞCA

CHARACTERIZATION OF NUCLEAR FUEL ROD CLADDING ZIRCONIUM ALLOYS

ABSTRACT

Zirconium alloys are very important for nuclear industry with their outstanding features. Due to enhanced mechanical and physical properties, Zircaloy-4 is the most popular zirconium alloy. Although zirconium alloys are produced by many techniques, cold rolling has been chosen for this study owing to its ease of use and cheapness. In this study, Zircaloy-4 rods are heat treated and cold rolled to different (15%, 30%, 45%, 60%, and 75%) reduction ratios to determine the effect of heat treatment and cold rolling on physical and mechanical properties.

X-ray diffractometer (XRD) is used for phase analysis, atomic force microscope (AFM) and surface roughness tester are used for surface analysis, scanning electron microscope (SEM) is used for fractography study, energy dispersive spectroscope (EDS) is used for elemental analysis, and optical microscope is used to examine the microstructure. Mechanical properties are investigated using universal mechanical tester (UMT) and micro Vickers hardness tester.

It is found that hardness increased with increasing reduction ratio. Increase in hardness altered the fracture from ductile to brittle. Surface roughness decreased with increasing reduction ratio. Oxygen absorption decreased with decreasing surface roughness. Absorbed oxygen did not create a new phase due to dissolving in interstitial positions. There is only Zr- α phase in all samples.

Keywords: Zirconium alloys, Zircaloy-4, nuclear fuel cladding, cold rolling, surface roughness, mechanical properties.

NÜKLEER YAKIT ÇUBUĞU ZİRKONYUM ALAŞIMLARININ KARAKTERİZASYONU

ÖZ

Zirkonyum alaşımları seçkin özellikleri ile nükleer endüstrisi için oldukça önemlidir. Gelişmiş mekanik ve fiziksel özellikleriyle Zircaloy-4 en çok bilinen zirkonyum alaşımıdır. Zirkonyum alaşımları birçok yöntemle üretiliyor olmasına rağmen kullanım kolaylığı ve ucuzluğu sebebiyle bu çalışmada soğuk haddeleme tercih edilmiştir. Bu çalışmada, ısıl işlem ve soğuk haddelemenin fiziksel ve mekanik özellikler üzerine etkilerini belirlemek için Zircaloy-4 çubuklara ısıl işlem ve farklı düşürme oranlarında (%15, %30, %45, %60 ve %75) soğuk haddeleme uygulanmıştır.

Faz analizi için X-ışını kırınım cihazı (XRD), yüzey analizi için atomik kuvvet mikroskobu (AFM) ve yüzey pürüzlülüğü test cihazı, kırık yüzey görüntüsü çalışmaları için taramalı elektron mikroskobu (SEM), element analizi için enerji dağılımlı spektroskopi (EDS) ve mikroyapıyı incelemek için optik mikroskop kullanılmıştır. Mekanik özelliklerin araştırılması içinse universal mekanik test cihazı (UMT) ve mikro Vickers test cihazı kullanılmıştır.

Düşürme oranının artışıyla sertliğin arttığı tespit edilmiştir. Sertlikteki artış kırılmanın sünekten gevreğe dönüşmesine sebep olmuştur. Yüzey pürüzlülüğü, düşürme oranının artışıyla azalmıştır. Yüzey pürüzlülüğü azaldıkça oksijen soğurma da azalmıştır. Soğurulan oksijen arayer pozisyonlarında çözündüğü için yeni bir faz oluşturmamıştır. Bütün numunelerde sadece Zr- α fazı bulunmaktadır.

Anahtar Kelimeler: Zirkonyum alaşımları, Zircaloy-4, nükleer yakıt zarfı, soğuk haddeleme, yüzey pürüzlülüğü, mekanik özellikler.

CONTENTS

M.Sc. THESIS EXAMINATION RESULT FORM	ii
ETHICAL DECLARATION	iii
ACKNOWLEDGMENTS	iv
ABSTRACT.....	v
ÖZ.....	vi
NOMENCLATURE	ix
LIST OF TABLES	x
LIST OF FIGURES	xi
CHAPTER 1 - INTRODUCTION	1
1.1 General Overview of Nuclear Reactors	2
1.1.1 Nuclear Reactor Types	3
1.1.2 Crucial Parts of Nuclear Reactors	15
1.2 Nuclear Fuel Rod Cladding Materials	18
1.2.1 M5	19
1.2.2 E110	19
1.2.3 ZIRLO	20
1.2.4 Zircaloy-2	20
1.2.5 Zircaloy-4	21
1.3 Aim of the Study	22
1.4 Review of Related Works	22
CHAPTER 2 - EXPERIMENTAL PROCEDURE	26
2.1 Heat Treatment	26
2.2 Cold Rolling	27
2.3 Sample Preparation	29
2.4 Surface Analysis	30
2.4.1 Surface Roughness Tester Measurements	31
2.4.2 AFM Measurements	31
2.5 Mechanical Analysis	32
2.5.1 Micro Vickers Hardness Tester Measurements	32
2.5.2 UMT Measurements	33
2.6 Microstructural Analysis.....	34

2.7 Elemental Analysis	35
2.8 Phase Analysis	35
2.9 Fractography Study	36
CHAPTER 3 - RESULTS AND DISCUSSION	37
3.1 Surface Roughness Tester Measurement Results	37
3.2 AFM Measurement Results	39
3.3 Micro Vickers Hardness Tester Measurement Results.....	48
3.4 UMT Measurement Results	50
3.5 Microstructural Analysis Results	56
3.6 Elemental Analysis Results	61
3.7 Phase Analysis Results.....	64
3.8 Fractography Study Results.....	66
CHAPTER 4 - CONCLUSIONS AND FUTURE WORK	70
4.1 Conclusions	70
4.2 Future Work	71
REFERENCES	73
CURRICULUM VITAE	81

NOMENCLATURE

Abbreviations

μm	Micrometer
mbar	Milibar
MPa	Megapascal
MW	Megawatt
N	Newton
nm	Nanometer
rpm	Rounds per minute

Acronyms

AFM	Atomic force microscope
AGR	Advanced gas-cooled reactor
BCC	Body-centered cubic
BWR	Boiling light-water reactor
CANDU	Canadian deuterium uranium reactor
EBR	Experimental breeder reactor
EDS	Energy dispersive spectroscopy
HCP	Hexagonal close-packed
HTGR	High temperature gas-cooled reactor
LMFBR	Liquid metal-cooled fast breeder reactor
MAGNOX	Magnesium alloy graphite moderated gas cooled UO ₂ reactor
PWR	Pressurized light-water reactor
RBMK	Reaktor bolshoy moshchnosti kanalniy
RD	Rolling direction
SEM	Scanning electron microscope
SGHWR	Steam generating heavy-water reactor
TD	Transverse direction
TRISO	Tristructural isotropic
UMT	Universal mechanical tester
VVER	Voda-vodyanoi energetichesky reactor
XRD	X-ray diffractometer

LIST OF TABLES

Table 1.1 Nuclear reactors in the world by nation (March 2015)	2
Table 1.2 Nuclear reactors in the world by type (March 2015).....	3
Table 1.3 Thermal neutron cross-sections of ^{10}B , ^{11}B , cadmium, and hafnium	17
Table 1.4 Physical properties of zirconium	18
Table 1.5 Chemical composition of M5	19
Table 1.6 Chemical composition of E110	19
Table 1.7 Chemical composition of ZIRLO	20
Table 1.8 Chemical composition of Zircaloy-2	20
Table 1.9 Chemical composition of Zircaloy-4	21
Table 1.10 Maximum impurity levels of Zircaloy-4	21
Table 2.1 Chemical composition of procured Zircaloy-4 rod.....	26
Table 2.2 Processes of Zircaloy-4 samples	26
Table 2.3 Chemical composition of etchant.....	30
Table 3.1 Elemental analysis results of samples	63

LIST OF FIGURES

Figure 1.1	Pressurized light-water reactor and intervals.....	4
Figure 1.2	Schematic representation of PWR power plant.....	5
Figure 1.3	Boiling light-water reactor and intervals	6
Figure 1.4	Schematic representation of BWR power plant	7
Figure 1.5	Schematic representation of internal working of a MAGNOX.....	8
Figure 1.6	Schematic representation of HTGR power plant	8
Figure 1.7	Coated fuel particles, fuel rod, and fuel element of HTGRs	9
Figure 1.8	Schematic representations of CANDU reactor and intervals	10
Figure 1.9	Schematic representations of RBMK reactor and intervals.....	11
Figure 1.10	Schematic representation of LMFBR power plant.....	12
Figure 1.11	Reactor vessel and intervals of pool type LMFBRs	13
Figure 1.12	Reactor vessel and intervals of loop type LMFBRs	14
Figure 1.13	Fuel element and fuel assembly for BWRs	15
Figure 1.14	Schematic picture of TRISO fuel particle	16
Figure 1.15	Schematic picture of control rod for a BWR.....	17
Figure 2.1	Heat treatment furnace used in annealing.....	27
Figure 2.2	Rolling machine	27
Figure 2.3	PROTHERM heat treatment furnace	28
Figure 2.4	Cold rolled samples.....	28
Figure 2.5	PRESI Mecatome T260 abrasive cutter	29
Figure 2.6	ATM Opal 460 hot mounting press	29
Figure 2.7	METKON Forcipol 2V grinder and polisher	30
Figure 2.8	MITUTOYO Surftest SJ-301 surface roughness tester	31
Figure 2.9	Park Systems XE-100E AFM.....	31
Figure 2.10	SHIMADZU HMV-G micro Vickers hardness tester	32
Figure 2.11	Diamond pyramid indenter and indentation mark	33
Figure 2.12	BRUKER UMT	33
Figure 2.13	Berkovich triangular pyramid indenter and indentation mark	34
Figure 2.14	NIKON Eclipse MA100 inverted optical microscope	35
Figure 2.15	PANalytical Empyrean XRD	35
Figure 2.16	FEI Quanta Feg SEM.....	36

Figure 3.1	Ra and Rz values of rolling direction of cold rolled samples.....	37
Figure 3.2	Ra values of rolling and transverse direction of etched samples	38
Figure 3.3	Rz values of rolling and transverse direction of etched samples	38
Figure 3.4	Ra values of samples in nanoscale	39
Figure 3.5	Schematic representation of etching mechanisms.....	39
Figure 3.6	Rz values of samples in nanoscale	40
Figure 3.7	Topography image of rolling direction of AR.....	41
Figure 3.8	Topography image of transverse direction of AR	41
Figure 3.9	Topography image of rolling direction of AN	42
Figure 3.10	Topography image of transverse direction AN	42
Figure 3.11	Topography image of rolling direction of CR15.....	43
Figure 3.12	Topography image of transverse direction of CR15	43
Figure 3.13	Topography image of rolling direction of CR30.....	44
Figure 3.14	Topography image of transverse direction of CR30.....	44
Figure 3.15	Topography image of rolling direction of CR45.....	45
Figure 3.16	Topography image of transverse direction of CR45	45
Figure 3.17	Topography image of rolling direction of CR60.....	46
Figure 3.18	Topography image of transverse direction of CR60.....	46
Figure 3.19	Topography image of rolling direction of CR75.....	47
Figure 3.20	Topography image of transverse direction of CR75	47
Figure 3.21	Microhardness values of samples after cold rolling.....	48
Figure 3.22	Microhardness values of samples after etching.....	49
Figure 3.23	Load-depth graphs of rolling and transverse directions of AR	50
Figure 3.24	Load-depth graphs of rolling and transverse directions of AN	51
Figure 3.25	Load-depth graphs of rolling and transverse directions of CR15	51
Figure 3.26	Load-depth graphs of rolling and transverse directions of CR30	52
Figure 3.27	Load-depth graphs of rolling and transverse directions of CR45	52
Figure 3.28	Load-depth graphs of rolling and transverse directions of CR60	53
Figure 3.29	Load-depth graphs of rolling and transverse directions of CR75	53
Figure 3.30	Load-depth graphs of rolling directions of samples.....	54
Figure 3.31	Load-depth graphs of transverse directions of samples.....	54
Figure 3.32	Average nanohardness values of samples after etching.....	55
Figure 3.33	Average elastic modulus values of samples	56

Figure 3.34	Surface photographs of rolling direction of samples	56
Figure 3.35	Microstructures of rolling and transverse directions of AR	57
Figure 3.36	Microstructures of rolling and transverse directions of AN	58
Figure 3.37	Microstructures of rolling and transverse directions of CR15	58
Figure 3.38	Microstructures of rolling and transverse directions of CR30	59
Figure 3.39	Microstructures of rolling and transverse directions of CR45	59
Figure 3.40	Microstructures of rolling and transverse directions of CR60	60
Figure 3.41	Microstructures of rolling and transverse directions of CR75	60
Figure 3.42	Average grain sizes of samples	61
Figure 3.43	SEM photograph (up) and graph of EDS result (down) for CR45	62
Figure 3.44	Characteristic XRD peaks of Zr- α	65
Figure 3.45	XRD peaks of samples.....	65
Figure 3.46	Fractography images of AR in 1000X (left) & 5000X (right)	66
Figure 3.47	Fractography images of AN in 1000X (left) & 5000X (right)	67
Figure 3.48	Fractography images of CR15 in 1000X (left) & 5000X (right)	67
Figure 3.49	Fractography images of CR30 in 1000X (left) & 5000X (right)	68
Figure 3.50	Fractography images of CR45 in 1000X (left) & 5000X (right)	68
Figure 3.51	Fractography images of CR60 in 1000X (left) & 5000X (right)	69
Figure 3.52	Fractography images of CR75 in 1000X (left) & 5000X (right)	69

CHAPTER 1

INTRODUCTION

Enrico Fermi and Leo Szilard invented the first nuclear reactor at the University of Chicago in 1942, 10 years after discovery of neutron by James Chadwick. Fermi and Szilard used chemically pure graphite moderator for decreasing the speed of neutrons to the fission speed. They utilized uranium oxide fuel and cadmium control rod to built first reactor of the United States. In the same year, Manhattan Project started with the consortium of United States, Great Britain, and Canada. Great Britain built Windscale nuclear reactors (Windscale Piles 1 and 2) in 1946. Metallic natural uranium was used in them to produce plutonium. These reactors were the least safe reactors among others. Windscale Pile 1 released 20000 curies of radiation because of becoming hot and firing of fuel in 1957. This accident was the second worst nuclear reactor accident in history. Before this accident, Great Britain developed its technology and built Calder Hall nuclear reactor with carbon dioxide cooling in 1956. This reactor was the first commercial nuclear reactor in the world [1].

The Union of Soviet Socialist Republics built the first civilian nuclear reactor named AM-1 in Obninsk in 1954. This reactor had water cooling together with graphite moderator and natural uranium fuel. Safety of this reactor was not good enough, so the Union of Soviet Socialist Republics improved new engineering skills and built channel type high power RBMK (reactor bolshoy moshchnosti kanalniy) reactors. The explosion of RBMK-4 near the Chernobyl town in 1986 was the worst nuclear reactor accident in history. Canada built a nuclear reactor research complex named NRX in Ontario in 1947 and experienced the world's first core meltdown in 1952. Heavy water was used as moderator and light water used for cooling in the Canadian nuclear reactor using natural uranium fuel. The United States concentrated on plutonium-fueled breeder reactors because of the lack of uranium fuel resources. Experimental breeder reactor one (EBR-1) was built in Idaho in 1951. This reactor was producing more plutonium than it consumed. An operator mistake caused a partial core meltdown in 1955 [1].

1.1 General Overview of Nuclear Reactors

There are many nuclear reactors all around the world with different types. Table 1.1 shows the nuclear reactors in the world.

Table 1.1 Nuclear reactors in the world by nation (May 2017) [2].

Nation	Operable	Under construction	Planned	Proposed	Total
Argentina	3	1	2	2	8
Armenia	1			1	2
Bangladesh			2		2
Belarus		2		2	4
Belgium	7				7
Brazil	2	1		4	7
Bulgaria	2			1	3
Canada	19		2		21
Chile				4	4
China	36	21	41	174	272
Czech Republic	6		2	1	9
Egypt			2	2	4
Finland	4	1	1		6
France	58	1			59
Germany	8				8
Hungary	4		2		6
India	22	5	20	44	91
Indonesia			1	4	5
Iran	1		4	7	12
Israel				1	1
Japan	42	2	9	3	56
Jordan			2		2
Kazakhstan				3	3
Korea DPR (North)				1	1
Korea RO (South)	25	3	8		36
Lithuania				2	2
Malaysia				2	2
Mexico	2			3	5
Netherlands	1				1
Pakistan	4	3			7
Poland			6		6
Romania	2		2		4
Russia	35	7	26	22	90
Saudi Arabia				16	16
Slovakia	4	2		1	7
Slovenia	1			1	2
South Africa	2			8	10
Spain	7				7
Sweden	9				9
Switzerland	5			3	8
Thailand				5	5
Turkey			4	8	12
Ukraine	15		2	11	28
United Arab Emirates		4		10	14
United Kingdom	15		11	2	28
United States	99	4	16	19	138
Vietnam			4	6	10
Total	441	62	169	373	1045

Nuclear technology accelerates the development of other technologies, so all countries are trying to pass others in this track. The United States, France, Japan, Russia, China, and Canada are the leading countries in the nuclear reactor technology.

1.1.1 Nuclear Reactor Types

There are six different types of nuclear reactors in the world. Table 1.2 shows the distribution of nuclear reactors by type.

Table 1.2 Nuclear reactors in the world by type (May 2017) [2].

Reactor Type	Main Countries	Operational	Planned / Under Construction	Total	Fuel
Pressurized light-water reactors (PWR)	The United States, France, Japan, and Russia	290	88	378	Enriched UO ₂
Boiling light-water reactors (BWR)	The United States, Japan, and Sweden	80	6	86	Enriched UO ₂
Gas-cooled reactors (MAGNOX)	The United Kingdom	15	1	16	Natural U (metal), enriched UO ₂
Pressurized heavy-water reactors (CANDU)	Canada	49	9	58	Natural UO ₂
Graphite-moderated light-water reactors (RBMK)	Russia	15		15	Enriched UO ₂
Liquid metal-cooled fast breeder reactors (LMFBR)	France and Russia	3	5	8	PuO ₂ and UO ₂

PWRs are the most commonly used nuclear reactors. The United States and France have the vast majority of PWRs in the world. Figure 1.1 shows the pressurized light-water reactor and intervals.

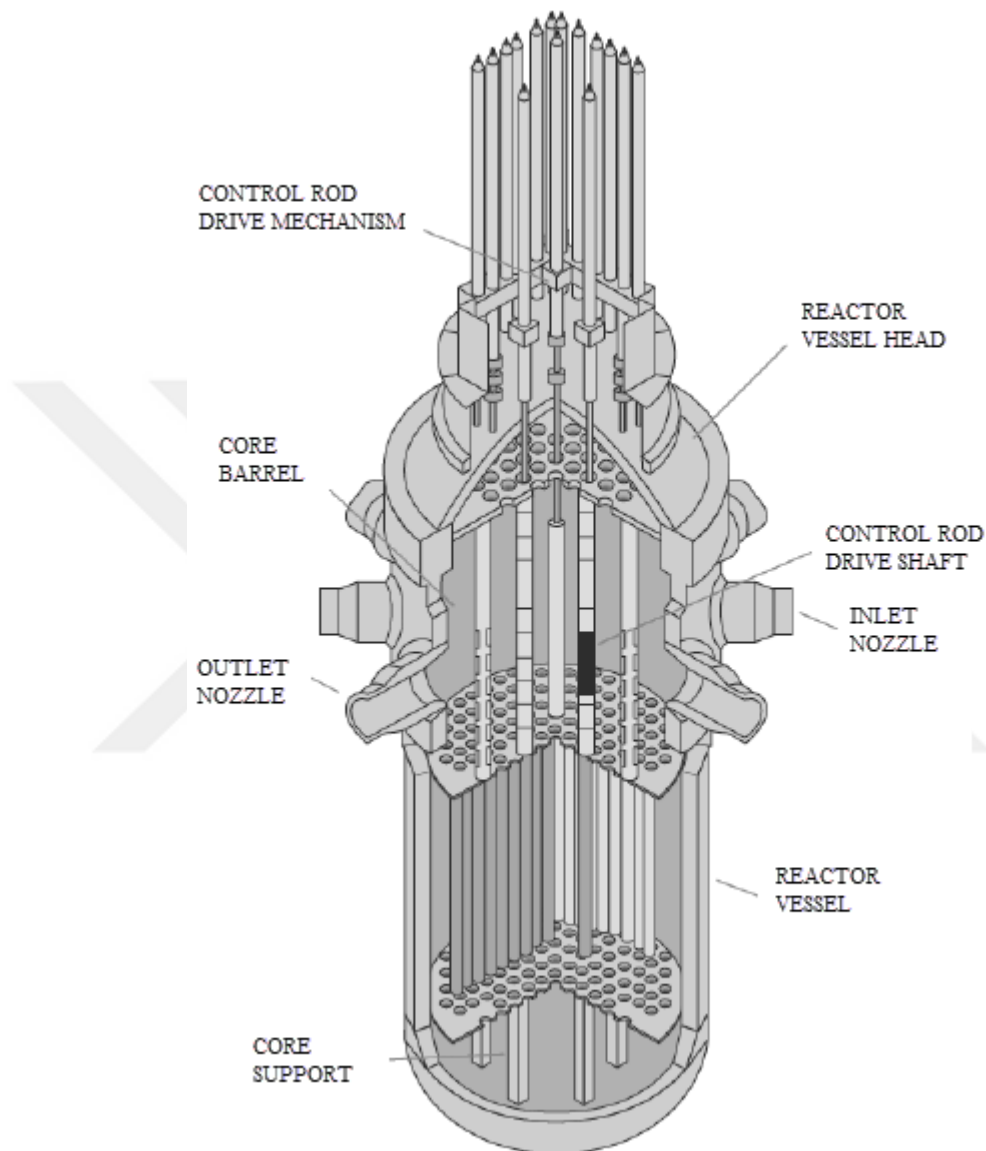


Figure 1.1 Pressurized light-water reactor and intervals [1].

The working principle of PWRs is all the same. Primary coolant collects steam to the steam generator and this steam stirs the turbine [3]. Control rod propulsion devices are combined with the upper reactor head. Vessel is made from low alloy carbon steel and have an inside cladding with austenitic stainless steel. The main

characteristic feature of PWRs is the high pressure about 15.5 MPa. Coolant water inlet and outlet temperatures are 293°C and 329°C, respectively. PWRs generate an average of 1300 MW of electrical power [4]. Schematic representation of pressurized light-water reactor power plant is shown in Figure 1.2.

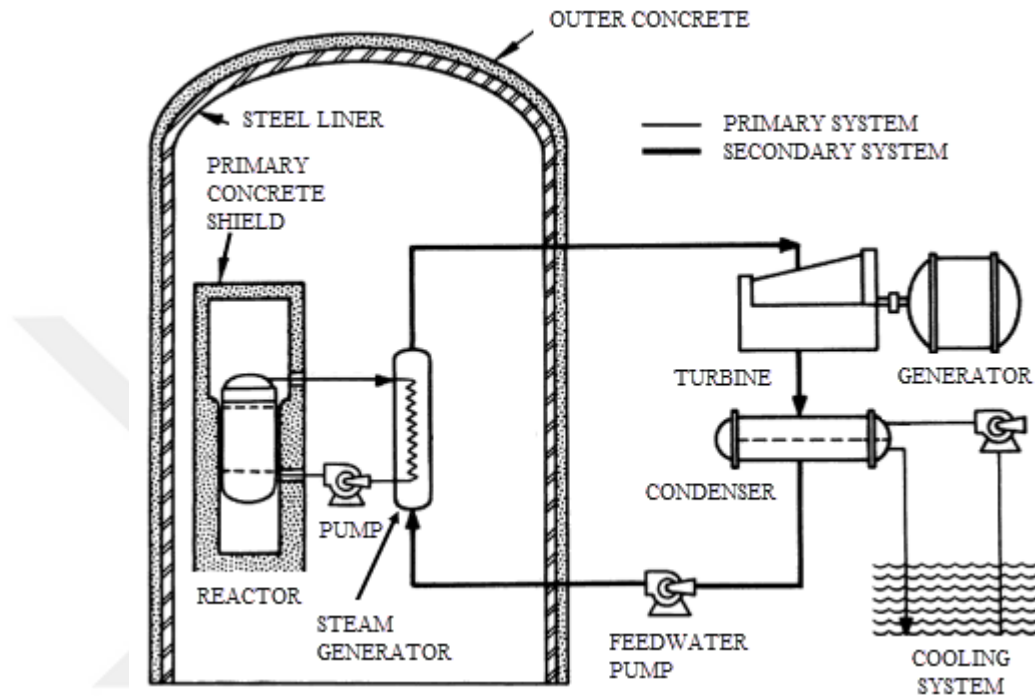


Figure 1.2 Schematic representation of PWR power plant [3].

PWRs contain approximately 110 tons of sintered UO_2 ceramic pellets in almost 40000 fuel rods. The ratio of hydrogen in water to uranium in fuel is a significant factor in the design of PWR core. Hydrogen/Uranium ratio adjusts the neutron spectrum. This spectrum influences the range of resonance capture and the fraction of fast-neutron fissions. Hydrogen/Uranium atomic ratio is about 4, so $\text{H}_2\text{O}/\text{UO}_2$ volumetric ratio is nearly 2 [3, 4].

BWRs come second in commonness after PWRs. The United States and Japan have nearly 70% of all BWRs in the world. Samuel Untermyer (a mechanical engineer from Massachusetts Institute of Technology) became the inventor of boiling light-water nuclear reactor by suggesting to boil the cooling water in the reactor core and eliminating external steam generator. Greater stability is provided by boiling of light-

water moderator in the reactor core. BWRs are probably the safest nuclear reactors in the world [1]. Figure 1.3 shows the boiling light-water reactor and intervals.

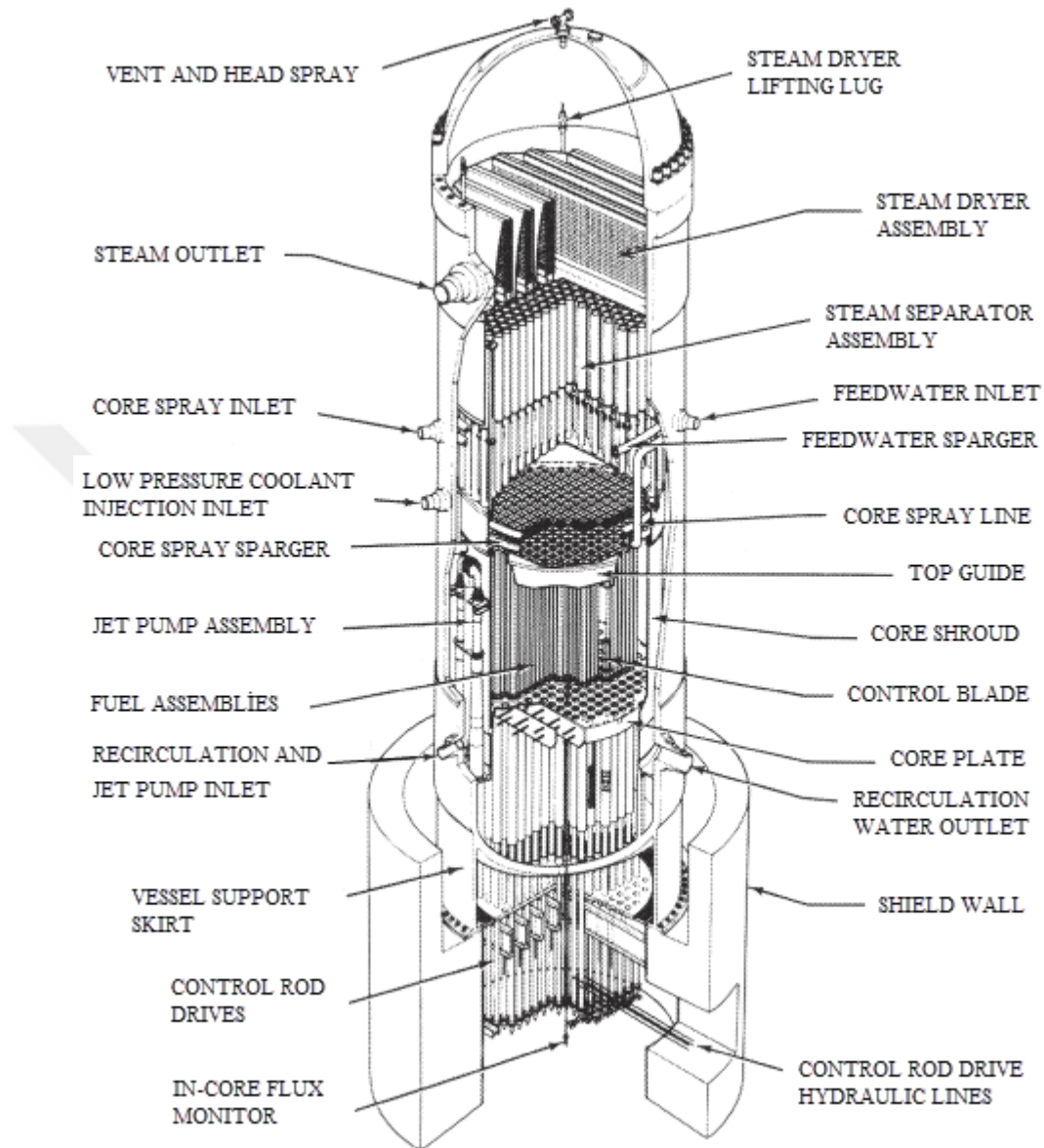


Figure 1.3 Boiling light-water reactor and intervals [3].

The working principle of BWRs is simpler than that of PWRs due to directly going of steam to the turbine. Nevertheless, keeping up the weight fraction of steam less than 14% for stability is a difficult issue [4].

BWRs produce approximately 1300 MW of electrical power with a system pressure of 7.17 MPa. Steam and feeding water temperatures are 289°C and 216°C, respectively. BWRs contain nearly 170 tons of UO_2 fuel filled in roughly 50000 fuel rods [4]. Schematic representation of boiling light-water reactor power plant is shown in Figure 1.4.

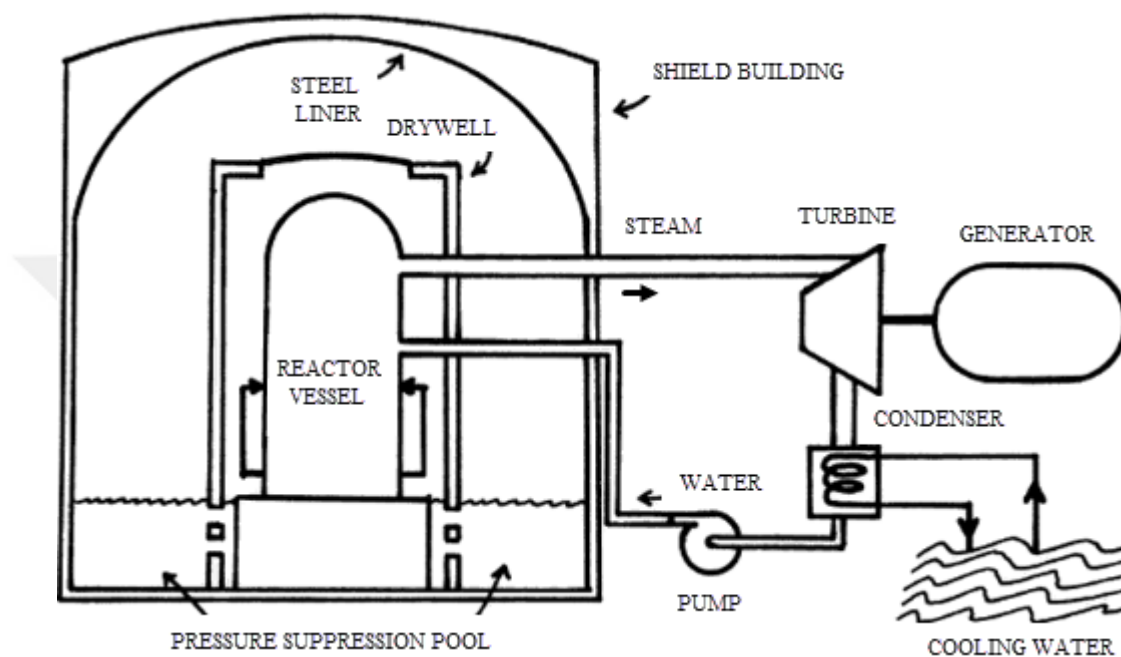


Figure 1.4 Schematic representation of BWR power plant [3].

Hydrogen/Uranium ratio affects the fission reaction like in PWRs. This ratio in BWRs is a little bit smaller than that for PWRs. In the meantime, $\text{H}_2\text{O}/\text{UO}_2$ volumetric ratio is higher than that of PWRs [4].

MAGNOX reactors have carbon dioxide gas coolant and graphite moderator. This design was chosen by Great Britain for economical and safety reasons. MAGNOX reactors were used for both electrical power generation and plutonium production. Plutonium production for military purposes was canceled in 1995 [1]. Metallic natural uranium was used as fuel with magnesium-aluminum alloy cladding [4]. MAGNOX reactors are all shut down now. Advanced gas-cooled reactors (AGRs) and PWRs are in use in Great Britain [1]. Figure 1.5 shows the schematic representation of internal workings of a MAGNOX reactor.

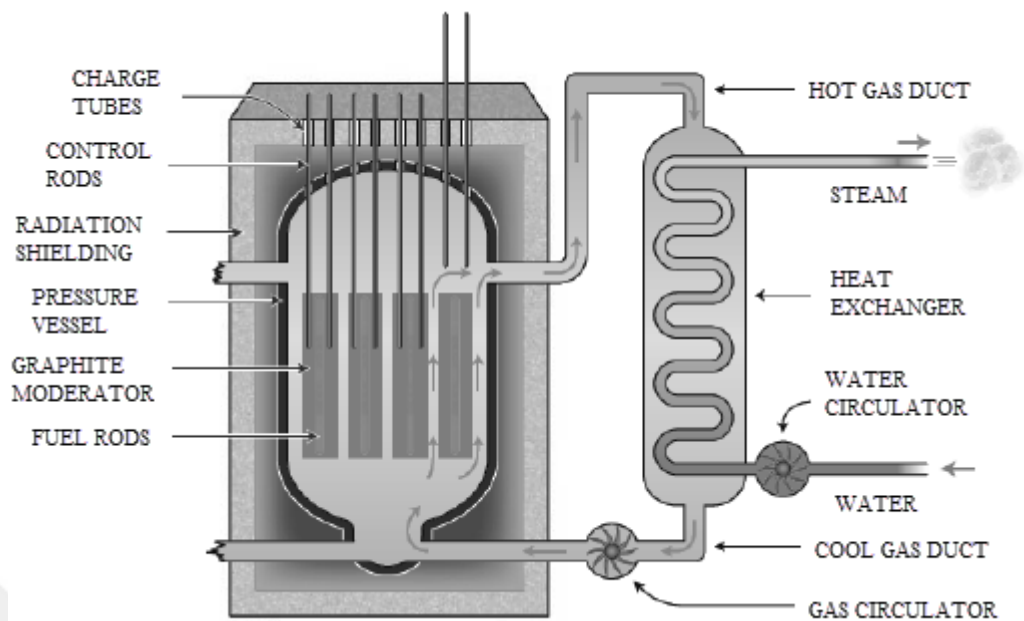


Figure 1.5 Schematic representation of internal working of a MAGNOX [1].

High temperature gas-cooled reactor (HTGR) is another type of graphite-moderated and gas-cooled reactors. Pressurized helium is used as coolant in HTGRs due to chemical inertness [4]. Uranium and thorium pellets are used as fuel by stacking into carbon moderator blocks of fuel regions [3]. Figure 1.6 shows the schematic representation of high temperature gas-cooled reactor power plant.

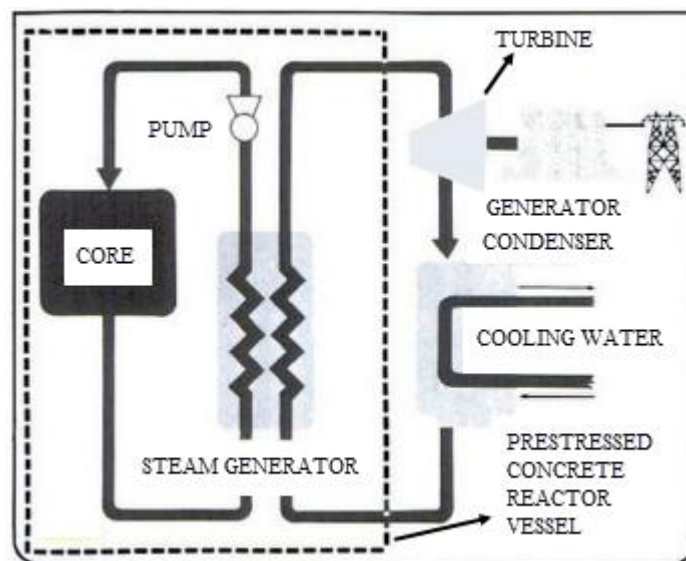


Figure 1.6 Schematic representation of HTGR power plant [3].

The fuel of HTGR consists of two components. Highly enriched uranium is used as fissile material, and thorium is used as fertile material. Both of these materials are in ceramic form. Highly enriched uranium core is coated with pyrolytic carbons and silicon carbide. On the other hand, thorium core is coated with carbon. Highly enriched uranium and thorium cores are combined with carbon binder and formed the fuel rod. Hereafter, fuel rods are stacked into hexagonal fuel elements [3]. Coated fuel particles, fuel rod, and fuel element of HTGRs are shown in Figure 1.7.

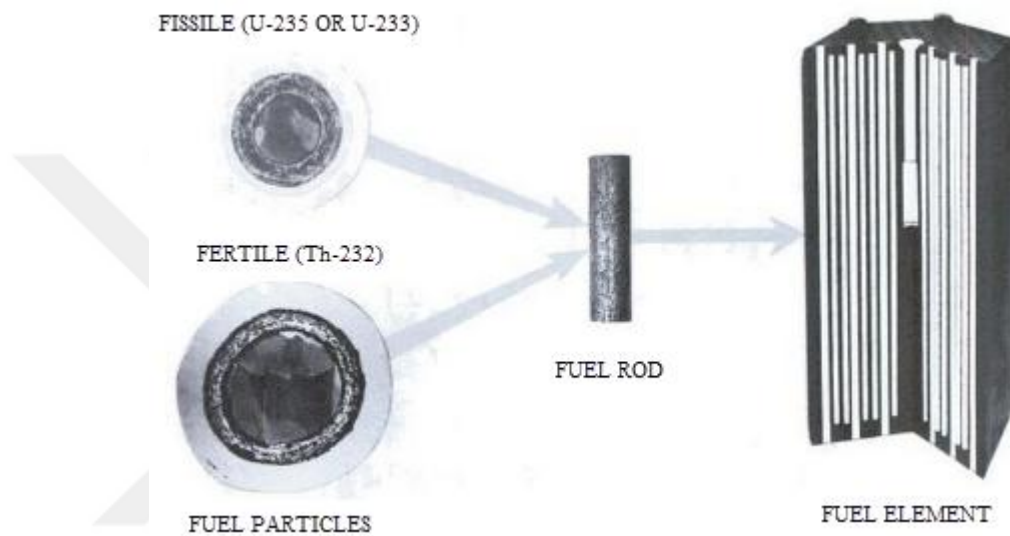


Figure 1.7 Coated fuel particles, fuel rod, and fuel element of HTGRs [3].

HTGRs produce nearly 1100 MW of electrical power with nearly 4000 fuel elements. The pressure of helium coolant is about 4.8 MPa. Inlet and outlet temperatures of coolant are 336°C and 741°C, respectively [3].

Heavy-water moderated reactors come third in terms of commonness. Canada has nearly 45% of heavy-water moderated reactors. These reactors are named CANDU (Canadian Deuterium Uranium) due to leadership of Canada in this technology [4].

Heavy-water is used as both coolant and moderator in CANDU reactors. Heavy-water coolant works under pressure to prevent the boiling; conversely, there is no need to pressurize the heavy-water moderator [4].

Consequently, heavy-water coolant and heavy-water moderator have completely separated circulation systems. The refueling of reactor without shutdown is one of the most important features of CANDU reactors [4].

Expensive construction and building materials are the main disadvantages of CANDU reactors. Purification of heavy-water to desired level is another economic difficulty [1]. Figure 1.8 shows the schematic representation of CANDU reactor and intervals.

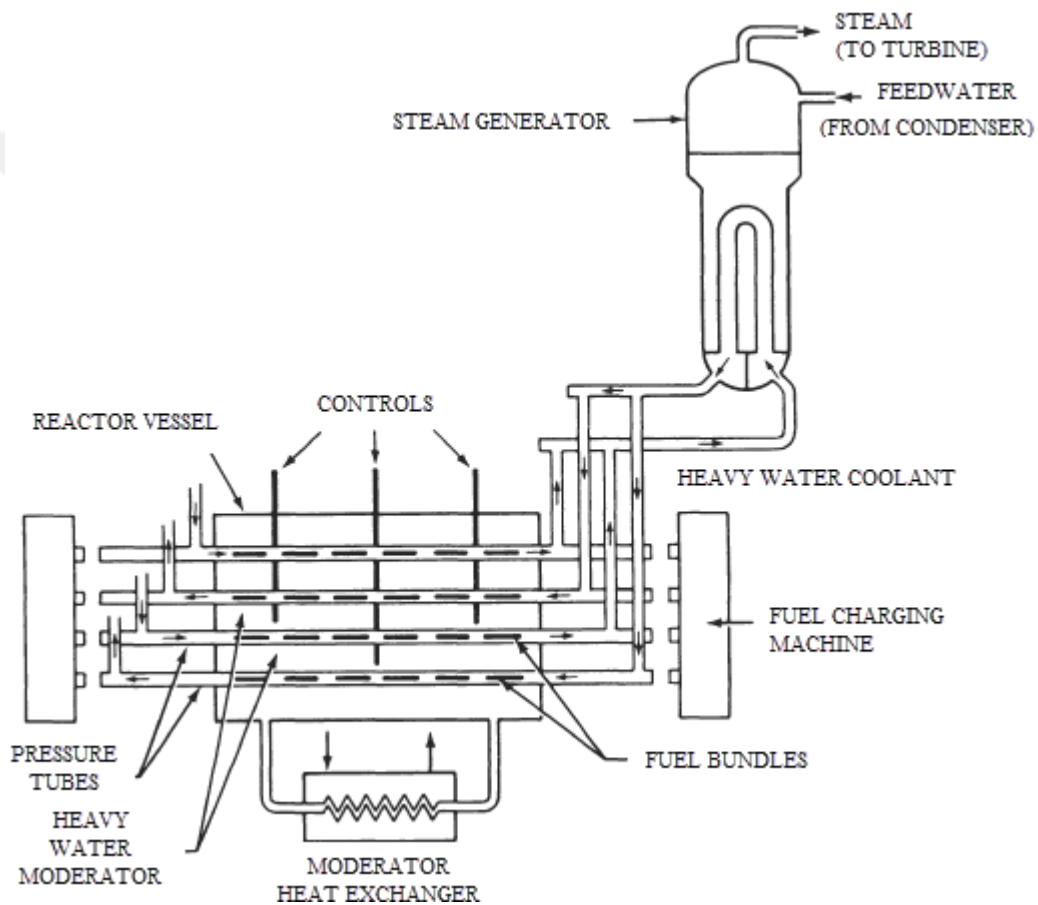


Figure 1.8 Schematic representations of CANDU reactor and intervals [4].

A typical CANDU reactor produces 600 MW of electrical power with nearly 100 tons of UO_2 fuel. Inlet and outlet pressures of heavy-water coolant are 11.3 MPa and 10 MPa, respectively. CANDU reactor uses almost 460 tons of heavy-water for both coolant and moderator [4].

Steam generating heavy-water reactor (SGHWR) design is similar to the CANDU with little differences. Heavy-water is used as moderator and light-water is used as coolant in SGHWRs. The light-water coolant is allowed to boil as in BWRs. The fuel of SGHWRs is poorly enriched uranium [3].

RBMKs (high-power channel reactor) are a different type of nuclear reactor with cylindrical graphite core and light-water coolant. Cylindrical graphite core is covered by a steel vessel filled with helium and nitrogen mixture. The light-water is permitted to boil as in BWRs. After boiling, steam passes through a steam separator to send the steam to the turbine and to recover the water in the steam-water mixture [5].

RBMKs are built in Russia, Ukraine, and Lithuania by the Union of Soviet Socialist Republics. Kursk, St. Petersburg, Smolensk, and Chernobyl nuclear reactors produced nearly 1000 MW while Ignalina nuclear reactor was producing 1500 MW of electrical power. Chernobyl RBMK nuclear reactors were all shutdown after the accident in 1986 [5]. Figure 1.9 shows the schematic representation of RBMK reactor and intervals.

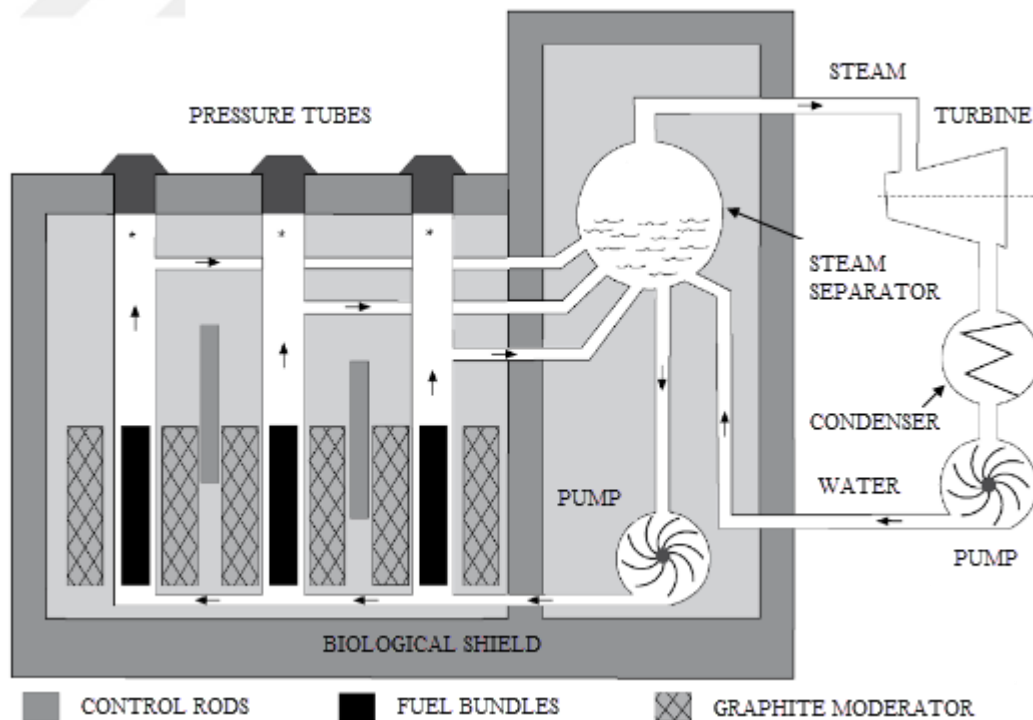


Figure 1.9 Schematic representations of RBMK reactor and intervals [6].

One of the main advantages of RBMKs is the online refueling as in CANDU reactors. However, RBMKs need a complete shutdown every 12 months for component maintenance and repair [7].

An important difference of RBMKs from other nuclear reactors is the absence of containment structure. RBMKs did not have containment structure due to economic reasons. Nevertheless, absence of containment structure increased the effect of Chernobyl disaster [7].

Liquid metal-cooled fast breeder reactors (LMFBRs) attracted more interest in France and Russia [1]. LMFBRs use liquid metal coolant, generally sodium. Heat is transferred from liquid metal sodium coolant to another sodium cycle by a heat exchanger. This second cycle of sodium works with a steam generator [3]. The schematic representation of liquid metal-cooled fast breeder reactor power plant is shown in Figure 1.10.

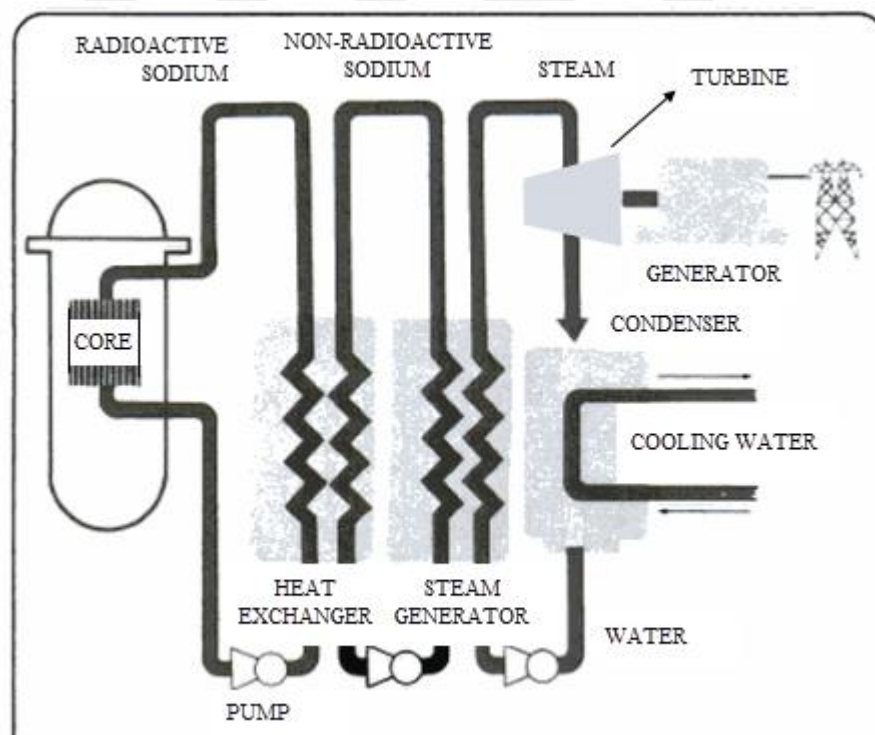


Figure 1.10 Schematic representation of LMFBR power plant [3].

LMFBRs need higher enrichment of uranium than BWRs. France built the first large scale LMFBR in 1984. LMFBRs have production capacity of 20% more fuel than it consumes [8]. PuO_2 and UO_2 are used as fuel inside steel cladding tubes [9].

LMFBRs produce almost 1500 MW of electrical power with nearly 40% power plant efficiency. The number of fuel rods used in this reactor is roughly 90000. Inlet and outlet temperatures of primary heat transport system are 385°C and 538°C , respectively. These temperature values are a bit lower in intermediate heat transport system [3].

There are two types of LMFBRs; pool type and loop type. The reactor core and some other components are collected in the reactor vessel in pool type LMFBRs. Using pool type in LMFBRs reduces the external pipe quantity [3]. The reactor vessel and intervals of a pool type liquid metal-cooled fast breeder reactor are shown in Figure 1.11.

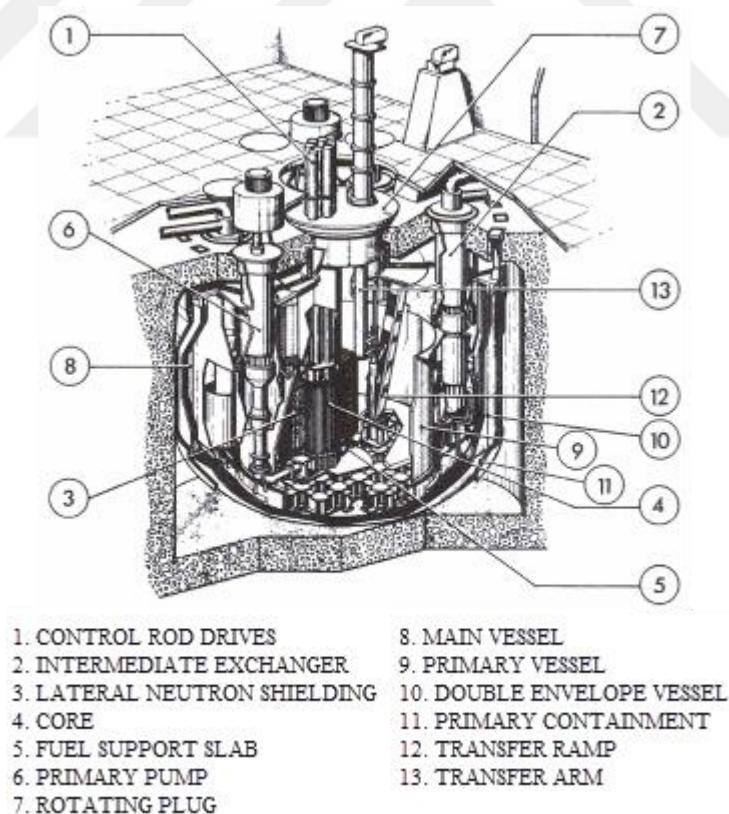


Figure 1.11 Reactor vessel and intervals of pool type LMFBRs [3].

The fuel lifetime of LMFBRs is a major question. Fissile loading more than 4% can damage the fuel and cladding material. Loop type of LMFBR is similar to light-water reactors. There is only core in the reactor vessel in LMFBRs. The heat transfer system of LMFBRs is connected to the reactor vessel by pipes [3]. The reactor vessel and intervals of a loop type liquid metal-cooled fast breeder reactor are shown in Figure 1.12.

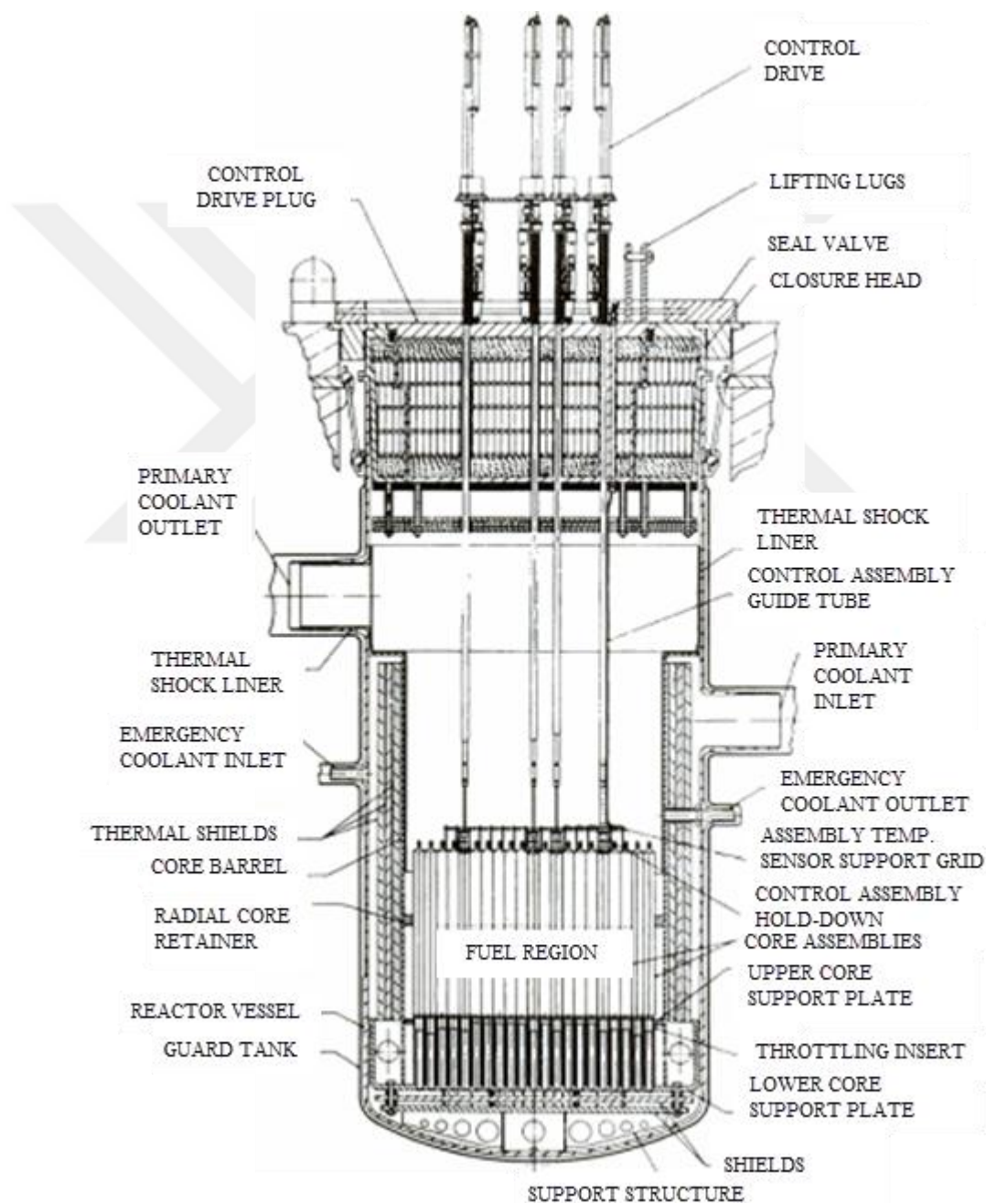


Figure 1.12 Reactor vessel and intervals of loop type LMFBRs [3].

1.1.2 Crucial Parts of Nuclear Reactors

Fuel elements are the most important parts of a nuclear reactor. Any fissionable material can be used as fuel in reactors. This fuel can be fissile material like ^{233}U , ^{235}U , ^{239}Pu , and ^{241}Pu . On the other hand, the fuel can be fissionable material like ^{232}Th , ^{238}U , and ^{240}Pu . These fuels are used in nuclear reactors in oxide, carbide, and nitride ceramic forms [10].

Fuel element is the smallest proofed unit of the fuel. The fuel element is a metal rod filled with ceramic pellets of fuel for BWRs, PWRs, and LMFBRs. Fuel assemblies are created by special ordering of fuel elements [10]. Figure 1.13 shows the fuel element and fuel assembly for BWRs.

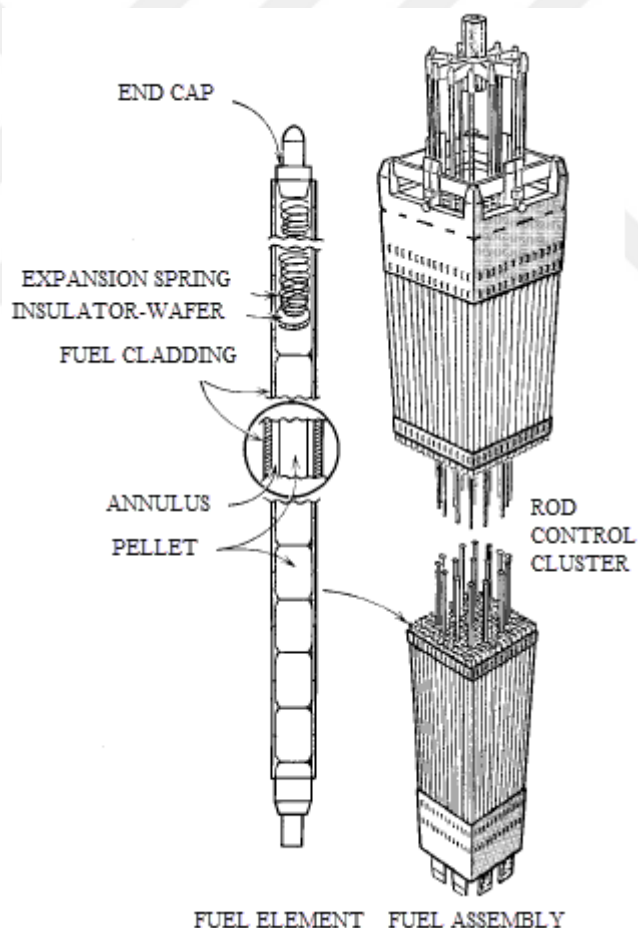


Figure 1.13 Fuel element and fuel assembly for BWRs [10].

The fuel element is small particles of pyrolytic graphite coated uranium carbide for HTGRs. Moreover, fuel assembly of HTGR is a hexagonal graphite block [10]. Figure 1.14 shows the schematic picture of TRISO (Tristructural isotropic) fuel particle for HTGRs.

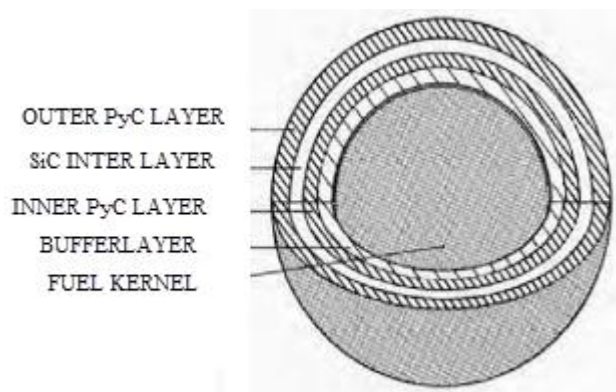


Figure 1.14 Schematic picture of TRISO fuel particle [11].

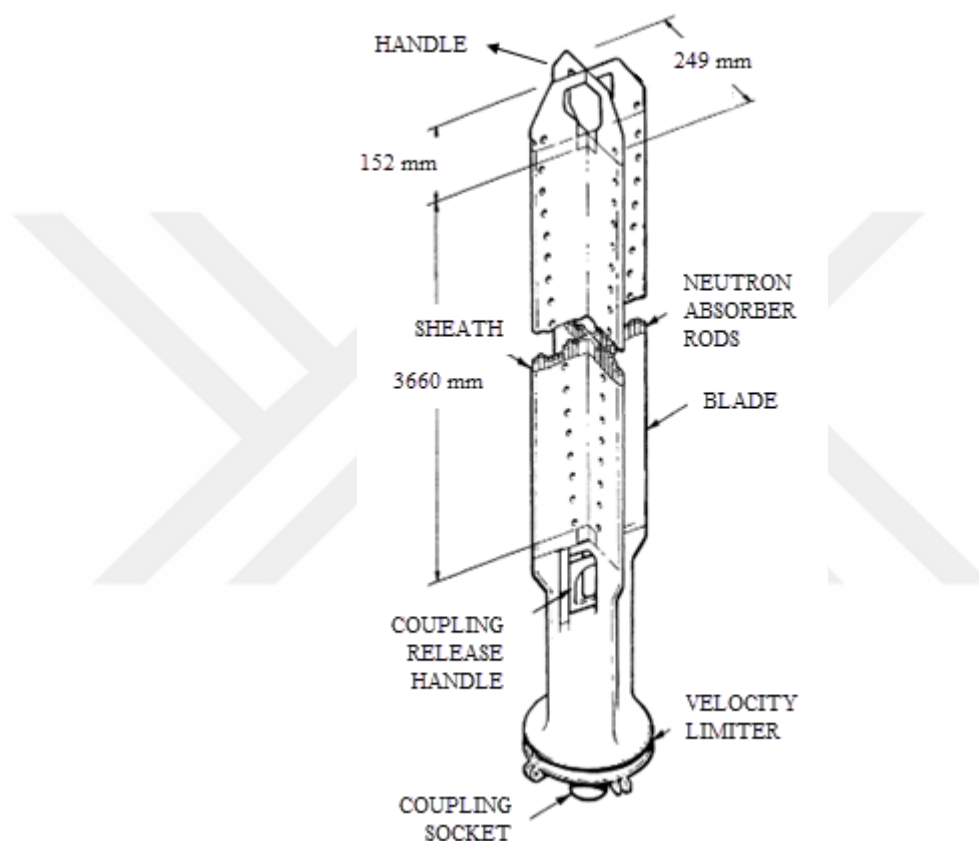
The TRISO fuel particle is coated with SiC and pyrolytic carbon layers. The core of this particle can be oxide, carbide or oxide-carbide mixture [11].

Control elements are as important as fuel elements. These materials are neutron-absorbing materials like cadmium, boron, and hafnium. Control element of a nuclear reactor can be in a rod form or in soluble poison form like boric acid. Soluble poison form can be used when the coolant is liquid. Soluble poisons are more advantageous than control rods due to ease of distribution [12]. The reactivity control can be provided partially with changing the boric acid concentration by dissolving in the liquid coolant. Nevertheless, this type of control is not as fast as control rod usage. For this reason, changing the boric acid concentration is used for long-term reactivity changes. However, using this technique decreases the number of control rods significantly [13]. Control rods are very important in reactivity control of many types of nuclear reactors. These rods are used for power stage alteration, the reactivity adjustment, and the quick stop of the reactor. The neutron absorber material for control rods is usually boron in the form of isotope ^{10}B [13]. Thermal neutron cross-section of ^{10}B is extremely higher than that of ^{11}B [4]. Table 1.3 shows the thermal neutron cross-sections of ^{10}B , ^{11}B , cadmium, and hafnium.

Table 1.3 Thermal neutron cross-sections of ^{10}B , ^{11}B , cadmium, and hafnium [4].

Element/Isotope	^{10}B	^{11}B	Cd	Hf
Cross-section (barns)	3837	0.0055	2520	104

Control rods can be located according to the design of the nuclear reactor. Control rods of PWRs are located on the top while BWRs have them located on the bottom of the reactor core [14].

**Figure 1.15** Schematic picture of control rod for a BWR [15].

An important feature of control material is staying stable after neutron capturing and not becoming radioactive. Cadmium was used as control material because of its ease of production. On the other hand, cadmium has low melting point and can be used only at low temperatures. Silver, indium, and cadmium alloy has higher melting point and larger neutron absorption cross-section than cadmium. After all, boron is the most used control material due to very high melting point and large neutron absorption cross-section [16].

1.2 Nuclear Fuel Rod Cladding Materials

Three Mile Island, Chernobyl, and Fukushima Daiichi nuclear power plant accidents showed the importance of nuclear fuel rod cladding materials. Although these nuclear power plants have different nuclear reactors (RBMK in Chernobyl, PWR in Three Mile Island, and BWR in Fukushima Daiichi), significance of fuel cladding material was the same for all of them [17].

There are different types of cladding materials such as magnesium-aluminum alloy, stainless steel, and zirconium alloys. Magnesium-aluminum alloy is used in MAGNOX reactors and stainless steel is used in AGRs. HTGRs work without nuclear fuel rod cladding. Zirconium alloys are used in all remaining reactors [1-4].

Excellent corrosion resistance, superior mechanical properties, and low thermal neutron cross-section make zirconium the best choice for nuclear fuel rod cladding material. Zirconium ores contain nearly 2.5% hafnium and it should be separated from zirconium for using in a nuclear reactor because of its very high neutron absorption cross-section [18].

Density of zirconium is lower than iron-based alloys. Thermal expansion coefficient of zirconium is 35% lower than that of titanium and 65% lower than that of stainless steel. Moreover, thermal conductivity of zirconium is 30% better than that of stainless steel [19]. Table 1.4 shows the physical properties of zirconium.

Table 1.4 Physical properties of zirconium [20-22].

Property	Value
Atomic number	40
Atomic weight	91.22
Density	6.5 g/cm ³
Melting point	1852°C
Boiling point	3580°C
Thermal neutron cross-section	0.18 barns
Crystal structure at 25°C	HCP
Crystal structure at 862°C	BCC
Thermal conductivity	22 W/mK
Thermal expansion coefficient	5.7 x 10 ⁻⁶ K ⁻¹

There are many zirconium alloys in service and used in investigations. However, only M5, E110, ZIRLO, Zircaloy-2, and Zircaloy-4 alloys are mentioned due to widespread use of them.

1.2.1 M5

M5 was developed as the fuel rod cladding material for PWRs by AREVA. This Zr-Nb-O ternary alloy has enhanced corrosion resistance with completely recrystallized structure [23]. Table 1.5 shows the chemical composition of M5.

Table 1.5 Chemical composition of M5 [24].

Element	Nb	O	Sn	Fe	Zr
Weight %	1	0.14	< 0.003	0.037	Balance

The homogenous distribution of Nb- β precipitates is one of the most important reasons for good creep resistance. Corrosion resistance and mechanical properties were improved by decreasing the amount of Sn and optimizing the heat treatment process. The addition of O about 900-1800 ppm increases the thermal creep resistance. On the other hand, the amount of C should be lower because of decreasing the steam-corrosion resistance [25].

1.2.2 E110

E110 has been used in Russian PWRs as nuclear fuel rod cladding material. This zirconium alloy has 1% Nb like the same that in M5 [26]. The chemical composition of E110 is shown in Table 1.6.

Table 1.6 Chemical composition of E110 [27].

Element	Nb	O	Sn	Fe	Zr
Weight %	1	-	-	-	Balance

The lack of alloying elements in E110 causes early α - β transition and influences the thermo-mechanical properties [28]. Russian scientists preferred addition of Nb instead of Sn due to positive effects to the cladding material [25]. E110 is designed for both RBMK and VVER (Voda-vodyanoi energetichesky reactor). High strength,

good creep resistance, and radiation growth resistance are typical properties of E110 [25].

1.2.3 ZIRLO

ZIRLO was developed for using in PWRs in 1987. This Zr-Nb-Sn-Fe alloy has better corrosion resistance, more favorable creep properties, and lower radiation growth than other Zr-Nb alloys [25]. Table 1.7 shows the chemical composition of ZIRLO.

Table 1.7 Chemical composition of ZIRLO [29].

Element	Nb	O	Sn	Fe	Zr
Weight %	1.8	-	1.2	0.1	Balance

Nb addition improves the mechanical properties without any increase in thermal neutron capture cross-section [30]. Moreover, Sn addition enhances strength and creep resistance [25]. The corrosion resistance of ZIRLO is better than others due to small-sized precipitates [31].

1.2.4 Zircaloy-2

Zircaloy-2 is the most commonly used nuclear rod cladding material in BWRs [32]. The steam corrosion resistance was improved by adding Fe, Ni, and Cr [25]. Table 1.8 shows the chemical composition of Zircaloy-2.

Table 1.8 Chemical composition of Zircaloy-2 [33].

Element	Ni	Cr	Sn	Fe	Zr
Weight %	0.05	0.1	1.5	0.14	Balance

Zircaloy-2 is in the form of stable α phase below 807°C and β phase above 977°C. Secondary phase precipitates can be seen in Zircaloy-2. Body-centered tetragonal Zr_2Ni or Zr_2Fe and hexagonal $ZrFe_2$ or $ZrCr_2$ are different types of secondary phase precipitates of Zircaloy-2 [34]. Hydrogen absorption is the main problem of Zircaloy-2. The effect of hydrogen absorption to the corrosion resistance is not important. On the other hand, its effect to the notch sensitivity is detrimental. Hydrogen absorption decreases the ductility of cladding to an unacceptable level [35].

1.2.5 Zircaloy-4

Chemical composition of cladding material is very important for hydrogen absorption. Zircaloy-2 had big problems about hydrogen absorption because of Ni content. Therefore, Ni-free Zircaloy-4 was developed to solve this problem [35]. Table 1.9 shows the chemical composition of Zircaloy-4.

Table 1.9 Chemical composition of Zircaloy-4 [36].

Element	O	Cr	Sn	Fe	Zr
Weight %	0.15	0.1	1.5	0.2	Balance

Zircaloy-4 has been a good material choice for PWRs since 1960s [37]. The addition of Fe and Cr improves the corrosion resistance. Thermal neutron capturing cross-section of Zircaloy-4 is very low like other zirconium alloy cladding materials [38]. Although there is no Ni in Zircaloy-4, H is still a big problem due to embrittlement. ZrO_2 is produced after corrosion of cladding with water and this reaction causes H production. H settles into solid solution until solubility limit. It precipitates after this limit and then influences the mechanical properties of Zircaloy-4 [39]. Some elements such as Hf should be removed to create nuclear grade material. Table 1.10 shows the maximum impurity levels of Zircaloy-4.

Table 1.10 Maximum impurity levels of Zircaloy-4 [35].

Element	Weight %
Aluminum	0.0075
Boron	0.00005
Cadmium	0.00005
Carbon	0.027
Copper	0.005
Hafnium	0.01
Hydrogen	0.0025
Magnesium	0.002
Molybdenum	0.005
Nickel	0.007
Nitrogen	0.008
Silicon	0.012
Tungsten	0.01
Uranium (total)	0.00035

1.3 Aim of the Study

Nuclear reactor technologies are very important and indispensable in today's world. Energy requirement is increasing with developing high technology. Nuclear power plants are the best solution with high energy production in relatively small areas. The most important parts of a nuclear reactor are fuel elements and control elements. The fissionable fuel, especially UO_2 , and the cladding material for the fuel are probably the most critical parts of fuel element.

The main purpose of this study is to make a contribution to Turkey's nuclear technology knowledge by getting in-depth information about physical and mechanical properties of Zircaloy-4 nuclear fuel rod cladding material.

In this study, the effect of heat treatment and cold rolling on physical and mechanical properties of Zircaloy-4 is investigated. Phase analysis, surface analysis, fractography study, elemental analysis, microstructural examination, and the investigation of mechanical properties are practiced to illustrate the effects of heat treatment and cold working on Zircaloy-4 specimens.

1.4 Review of Related Works

Mechanical properties of Zircaloy-4 have been investigated by many researchers since its development. Effect of heat treatment on microstructure of cladding material is another research topic that attracts the scientist's attention. Moreover, there are a great number of investigations about cold rolling of Zircaloy-4 nuclear fuel rod cladding material.

Yoo and Kim [40] have investigated the effect of texture changes on the 0.2% yield strength of quenched Zircaloy-4. They found that the enhancement in the 0.2% yield strength based upon the microstructural changes. The effect of texture change was very little.

In another study, Dupim et al. [41] have investigated hydrogen absorption and desorption kinetics of Zircaloy-4. They also studied the effect of cold rolling on

absorption and desorption reaction rates. They found that cold rolling significantly increases the hydrogen absorption kinetics and substantially decreases the hydrogen desorption temperature.

Fuloria et al. [42] have studied the effect of cold rolling on the hardness and tensile strength of Zircaloy-4. They found that the cold rolling increases the hardness and strength due to increasing of dislocation density and grain refinement. They also found that dislocation density increased with increasing stacking fault probability.

Cockeram and Hollenbeck [43] have investigated the effect of stress state on the deformation and fracture mechanism of Zircaloy-4. They performed their tests in both hydrided and non-hydrided conditions. They found that the stress to initial plastic deformation ratio increased and strain to failure ratio decreased due to high triaxiality values.

In another study, Steinbrück et al. [44] have investigated high temperature oxidation and quench behavior of Zircaloy-4. They also studied E110 zirconium alloy and made a comparison between Zircaloy-4 and E110. They found that oxidation, hydrogen absorption, hydrogen embrittlement behavior, and breakaway temperature were different for two zirconium alloys.

Lim et al. [45] have studied the effect of cold rolling and heat treatment on the mechanical properties of Zircaloy-4. It is claimed that texture was developed with higher rolling reduction and it was influenced by final heat treatment. It is also reported that the direction of the test affected the creep strain.

Gloaguen et al. [46] have reported the distribution of residual stress in cold rolled Zircaloy-4. They also tested a method for the detection of stress gradients. It is found that there is a complementation between grazing incidence diffraction and elastoplastic self-consistent models.

Busser et al. [47] have investigated mechanical properties and oxide layer damage evolution in Zircaloy-4 by ring compression test technique. They found that the ring compression test technique has an important potential for both analyzing the

mechanical properties of irradiated and non-irradiated nuclear fuel rod cladding materials.

In another study, Samal et al. [48] have studied failure behavior of stress-relief annealed Zircaloy-4 and recrystallization annealed Zircaloy-2. It is found that initiation fracture toughness and crack growth resistance of Zircaloy-2 were better than that of Zircaloy-4. They also found that the reason for high fracture toughness of Zircaloy-2 is fine-grained microstructure and low dislocation density.

Berger et al. [49] have reported the high temperature oxidation behavior of Zircaloy-4 under applied load. They found that the nuclear microanalysis method is a good choice for investigating the high temperature oxidation behavior due to capability of getting localized information.

De Menibus et al. [50] have investigated the fracture behavior of cold worked and stress relieved Zircaloy-4 nuclear fuel rod claddings with and without hydride blisters. They found that the increasing of biaxiality level decreased the ductility without hydride blisters. Moreover, it is reported that the fracture strain decreases with increasing of hydride blister depth.

Cockeram and Chan [51] have studied in situ deformation and fracture behavior of wrought Zircaloy-4 and Zircaloy-2 in different triaxialities. They also developed a micromechanical model to illustrate the ductile tearing mechanism. They compared experimental data with the results of the model and there were a good agreement between them. It is found that nucleation, growth, and coalescence of voids are dominant mechanisms of fracture.

In another study, Tong and Britton [52] have reported the generation of very large grains by deformation and heat treatment. They found that the texture of grains is affected by twinning mechanism. They also illustrated that the deformation level has a key role on nucleation, growth, and texture of very large grains.

Kim et al. [53] have investigated the failure behavior of Zircaloy-4 nuclear fuel rod cladding by simulated loss of coolant accident and mechanical tests. They oxidized

the cladding in steam atmosphere and quenched with cold water. They also investigated the ductility of oxidized and quenched samples by ring compression and three point bending tests.

Jung and Kim [54] have studied the effect of β heat treatment on microstructure and mechanical properties of Zircaloy-4 nuclear fuel cladding material. They reported that β heat treatment affected the morphology of microstructure by changing forms of β and α grains. They also found that the increase in heat treatment temperature decreased the yield strength.

Coindreau et al. [55] have investigated air oxidation of Zircaloy-4 cladding by a new model based on available experimental data obtained from IRSN and Karlsruhe. They found that the results of model were in a good agreement with experimental data.

In another study, Matsunaga et al. [56] have studied the plastic strain accumulation of Zircaloy-4 at room temperature to illustrate the mechanical characteristics of cladding. They found that the source of plastic strain accumulation is the heterogeneous dislocation structure. They also found that the interactions between dislocations limit the work-hardening behavior of Zircaloy-4 fuel cladding under constant load at room temperature due to plastic strain accumulation.

CHAPTER 2

EXPERIMENTAL PROCEDURE

Zircaloy-4 used in this study is procured from Nanografi Nanotechnology Ltd. in the form of rod with 10 mm diameter. Chemical composition of procured Zircaloy-4 rod is shown in Table 2.1.

Table 2.1 Chemical composition of procured Zircaloy-4 rod.

Element	O	Cr	Sn	Fe	Zr
Weight %	0.16	0.13	1.7	0.24	Balance

Zircaloy-4 rod is cut into 7 pieces and one of them is separated. This as-received sample named AR. Other 6 pieces of Zircaloy-4 rod are annealed and one of them is again separated. This annealed sample named AN. Remaining 5 pieces are cold rolled to 15%, 30%, 45%, 60%, and 75% reduction ratios and these samples named CR15, CR30, CR45, CR60, and CR75, respectively. Table 2.2 shows the processes of Zircaloy-4 samples.

Table 2.2 Processes of Zircaloy-4 samples.

Sample	AR	AN	CR15	CR30	CR45	CR60	CR75
Annealing (°C)	-	700	700	700	700	700	700
Cold rolling (%)	-	-	15	30	45	60	75

Metallographic processes are examined to each sample to make prepared them to following investigations. Surface analysis, mechanical analysis, microstructural analysis, elemental analysis, phase analysis, and fractography study are performed to illustrate physical and mechanical properties of Zircaloy-4 samples. Each step of experimental procedure is explained in detail.

2.1 Heat Treatment

The air in the furnace is removed by PREIFFER Hi-CUBE vacuum pump with 60 mbar vacuum before filling the atmosphere of the furnace with argon. As-received Zircaloy-4 rods, except AR, are annealed by applying 4 hours recrystallization heat

treatment at 700°C in argon atmosphere and cooling to room temperature in the furnace. Annealing process is performed by the furnace shown in Figure 2.1 in Middle East Technical University, metallurgical and materials engineering department.



Figure 2.1 Heat treatment furnace used in annealing.

2.2 Cold Rolling

CR15, CR30, CR45, CR60, and CR75 samples cold rolled to 15%, 30%, 45%, 60%, and 75% reduction ratios, respectively. 15% reduction ratio is practiced in each pass. Thereby, 1 pass for CR15, 2 passes for CR30, 3 passes for CR45, 4 passes for CR60, and 5 passes for CR75 are performed by two rolling mills, each has 240 mm diameter, at 1.25 rpm. Figure 2.2 shows the rolling machine in Gazi University, metallurgical and materials engineering department.



Figure 2.2 Rolling machine.

All samples are heated to 300°C before each pass. Heating operation is practiced in air atmosphere by PROTHERM heat treatment furnace shown in Figure 2.3.



Figure 2.3 PROTHERM heat treatment furnace.

Cold rolled samples cooled to room temperature in air atmosphere after last pass. Cold rolling caused contraction in width and expansion in length. Figure 2.4 shows cold rolled samples.



Figure 2.4 Cold rolled samples.

2.3 Sample Preparation

All samples are sectioned both from rolling direction (RD) and transverse direction (TD) to illustrate the anisotropy in the mechanical properties. Sectioning operation is practiced in Ankara Yıldırım Beyazıt University, material engineering department by PRESI Mecatome T260 abrasive cutter shown in Figure 2.5.



Figure 2.5 PRESI Mecatome T260 abrasive cutter.

Sectioned samples mounted into bakelite by ATM Opal 460 hot mounting press. This process is practiced in Gazi University, metallurgical and materials engineering department. Hot mounting press is shown in Figure 2.6.



Figure 2.6 ATM Opal 460 hot mounting press.

After hot mounting, mounted samples are grinded with 320, 600, 800, 1000, 1200, 2000, and 2500 grit SiC coated abrasive grinding papers. After this, samples are polished with 6 μm , 3 μm , and 1 μm diamond suspension on flocked polishing cloth. Grinding and polishing processes are performed in Ankara Yıldırım Beyazıt University, material engineering department by METKON Forcipol 2V grinder and polisher shown in Figure 2.7.



Figure 2.7 METKON Forcipol 2V grinder and polisher.

Polished samples are etched with proper etchant for thirty seconds to reveal the microstructure clearly. Chemical composition of etchant is shown in Table 2.3.

Table 2.3 Chemical composition of etchant.

Matter	Weight %
Hydrofluoric acid (HF)	10
Nitric acid (HNO ₃)	45
Distilled water	45

Grinding, polishing, and etching steps are repeated until achieving the desired quality of microstructural appearance.

2.4 Surface Analysis

Sample surfaces are investigated both in microscale and nanoscale. Microscale investigation is practiced by surface roughness tester, and nanoscale investigation is done by AFM (atomic force microscope).

2.4.1 Surface Roughness Tester Measurements

Surface roughness of samples is measured by MITUTOYO Surftest SJ-301 surface roughness tester with 5 x 0.8 mm mode in mechanical engineering department of Ankara Yıldırım Beyazıt University. Microscale roughness measurements are performed both just after cold rolling process and after etching. Transverse direction surface of cold rolled samples were not straight as shown before in Figure 2.4. For this reason, microscale surface roughness test is practiced only with rolling direction surface in cold rolled samples. Figure 2.8 shows the surface roughness tester.



Figure 2.8 MITUTOYO Surftest SJ-301 surface roughness tester.

2.4.2 AFM Measurements

Nanoscale surface roughness test is performed with rolling and transverse directions of polished and etched samples. Surface roughness of samples is measured by Park Systems XE-100E AFM with contact mode on 5 μm x 5 μm surface area. Moreover, surface topography of samples is obtained by same measurement. Figure 2.9 shows the AFM in Erzincan University.

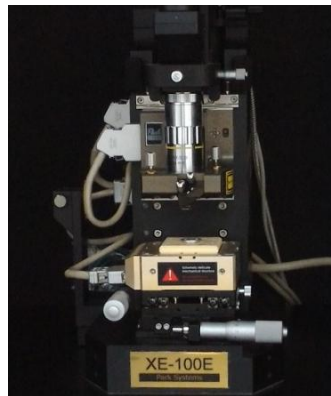


Figure 2.9 Park Systems XE-100E AFM.

2.5 Mechanical Analysis

Mechanical properties of samples are examined in both microscale and nanoscale. Microscale study is practiced by micro Vickers hardness tester, and nanoscale study is performed by UMT (universal mechanical tester).

2.5.1 Micro Vickers Hardness Tester Measurements

Microscale mechanical properties are examined with SHIMADZU HMV-G micro Vickers hardness tester in material engineering department of Ankara Yıldırım Beyazıt University. Microhardness test is practiced both just after cold rolling process and after polishing and etching. Microhardness measurements are practiced under 9.807 N load and 6 seconds holding time by diamond pyramid indenter. Figure 2.10 shows SHIMADZU HMV-G micro Vickers hardness tester.

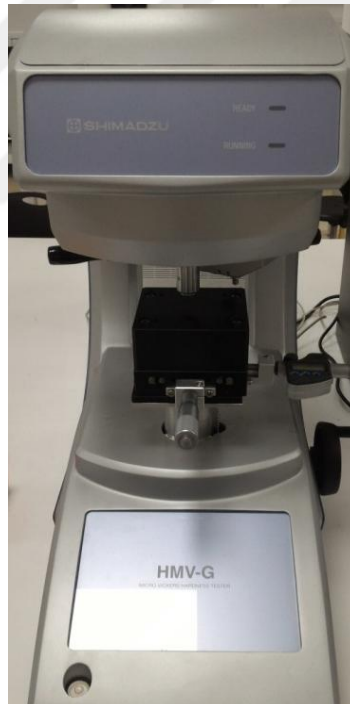


Figure 2.10 SHIMADZU HMV-G micro Vickers hardness tester.

The schematic representations of diamond pyramid indenter and indentation mark are shown in Figure 2.11.

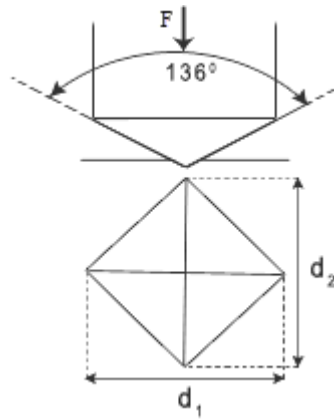


Figure 2.11 Diamond pyramid indenter and indentation mark.

The micro Vickers hardness equation (Eq. 2.1) can be written as follows:

$$\text{Micro Vickers hardness} = \frac{2F \sin \frac{136^\circ}{2}}{\left(\frac{d_1 + d_2}{2}\right)^2} \quad (2.1)$$

2.5.2 UMT Measurements

Nanoscale mechanical properties are studied by BRUKER UMT via nanoindentation test mode in Erzincan University. Rolling and transverse directions of samples are investigated after polishing and etching. BRUKER UMT is shown in Figure 2.12.

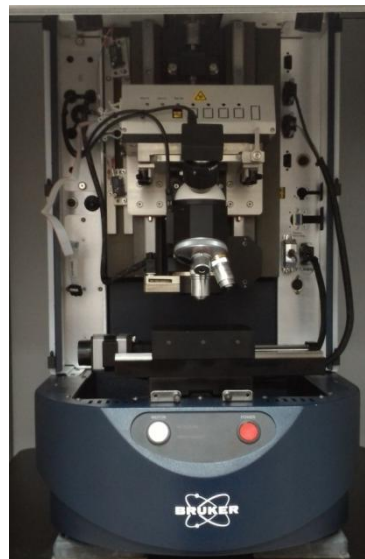


Figure 2.12 BRUKER UMT.

Nanoindentation tests are carried out by berkovich diamond triangular pyramid indenter with 100 nm tip radius. 50, 100, 150, 200, 250, 300, 350, and 400 mN loads are applied to each sample. Figure 2.13 shows the indenter and indentation mark.

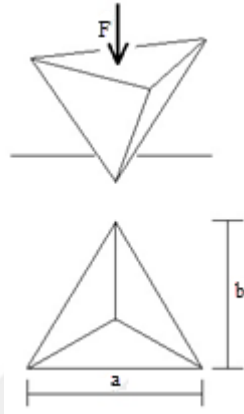


Figure 2.13 Berkovich triangular pyramid indenter and indentation mark.

Oliver and Pharr model is used in nanohardness calculations [57]. Berkovich nanohardness equation (Eq. 2.2) can be written as follows:

$$\text{Berkovich nanohardness} = \frac{2F}{ab} \quad (2.2)$$

2.6 Microstructural Analysis

Microstructure photographs of etched samples are taken by NIKON Eclipse MA100 inverted optical microscope in 1000X magnification to illustrate the grain structure, orientation, and size.

Moreover, surface photographs of rolling direction of samples are taken in 100X magnification to illustrate the effect of cold rolling reduction ratio on surface roughness. Furthermore, average grain sizes of samples are calculated by Clemex Vision Lite software. Figure 2.14 shows the inverted optical microscope.



Figure 2.14 NIKON Eclipse MA100 inverted optical microscope.

2.7 Elemental Analysis

Elemental analysis is examined by EDAX TEAM EDS (energy dispersive spectroscopy) analysis system attached to SEM (scanning electron microscope) in Erzincan University. Examined areas are chosen randomly in 10000X magnification. Results are illustrated via TEAM EDS software suite.

2.8 Phase Analysis

Phase analysis of samples is carried out by PANalytical Empyrean XRD (X-ray diffractometer) with Cu anode material in Erzincan University. Scanning is practiced between 30° and 85° at room temperature. PANalytical Empyrean XRD is shown in Figure 2.15.



Figure 2.15 PANalytical Empyrean XRD.

2.9 Fractography Study

Fracture surface pictures of samples are taken by FEI Quanta Feg 450 SEM in Erzincan University. Scanning is performed in 1000X and 5000X magnification with high vacuum mode. Scanned areas of fracture surfaces are chosen randomly. FEI Quanta Feg 450 SEM is shown in Figure 2.16.



Figure 2.16 FEI Quanta Feg 450 SEM.

CHAPTER 3

RESULTS AND DISCUSSION

3.1 Surface Roughness Tester Measurement Results

Transverse direction of samples was not straight after cold rolling as mentioned before. Therefore, microscale surface roughness measurement is applied to rolling direction of samples only. Surface roughness test results are presented by Ra and Rz values. Ra is the average value of all peaks and valleys in roughness profile. On the other hand, Rz is the average value of differences between 5 maximum peaks and 5 minimum valleys [58]. Figure 3.1 shows Ra and Rz values of rolling direction of cold rolled samples.

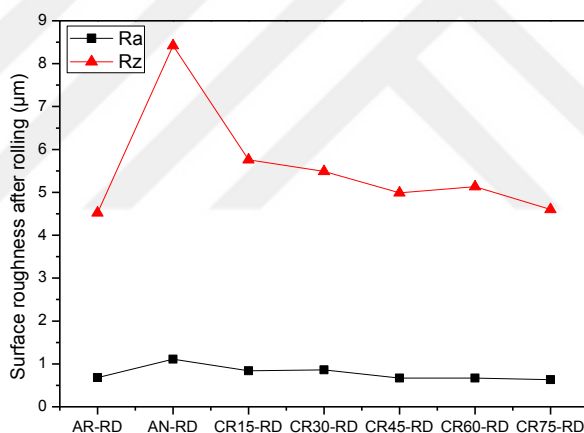


Figure 3.1 Ra and Rz values of rolling direction of cold rolled samples.

As seen in Figure 3.1, AN-RD has the highest Ra and Rz values, and these values are decreasing with increasing rolling reduction ratio. In other words, cold rolling reduced the surface roughness. Ra and Rz values of AR-RD, AN-RD, CR15-RD, CR30-RD, CR45-RD, CR60-RD, and CR75-RD are 0.68, 1.11, 0.84, 0.86, 0.67, 0.63 μm , and 4.52, 8.42, 5.76, 5.49, 4.99, 5.13, 4.60 μm , respectively. Ra and Rz values of AR-RD are close to samples with high rolling reduction ratio. The well known production route for rod shaped materials includes hot extrusion, multiple cold rolling, and annealing [59].

It is predicted that AR cold rolled to approximately 60% reduction ratio during fabrication. Microscale surface roughness test is performed after polishing and etching to illustrate the effect of polishing and etching on surface roughness. Figure 3.2 shows Ra values of rolling and transverse direction of etched samples.

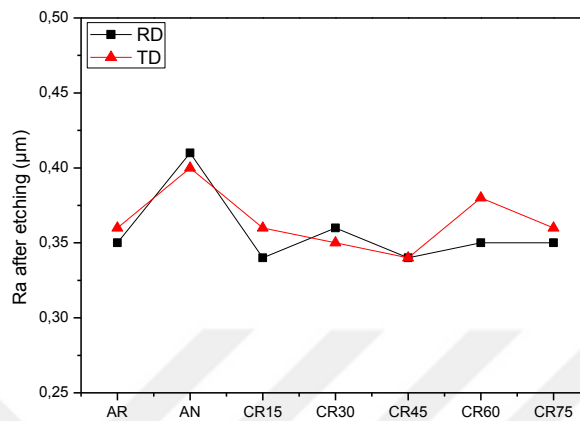


Figure 3.2 Ra values of rolling and transverse direction of etched samples.

If Figure 3.1 and Figure 3.2 are analyzed together, it can be deduced that polishing and etching reduced the Ra values in rolling direction. Ra values of rolling direction and transverse direction of AR, AN, CR15, CR30, CR45, CR60, and CR75 are 0.35, 0.41, 0.34, 0.36, 0.34, 0.35, 0.35 µm, and 0.36, 0.40, 0.36, 0.35, 0.34, 0.38, 0.36 µm, respectively. The little difference of Ra values among samples is derived from human error in polishing and etching steps. Rz values of rolling and transverse direction of etched samples are shown in Figure 3.3.

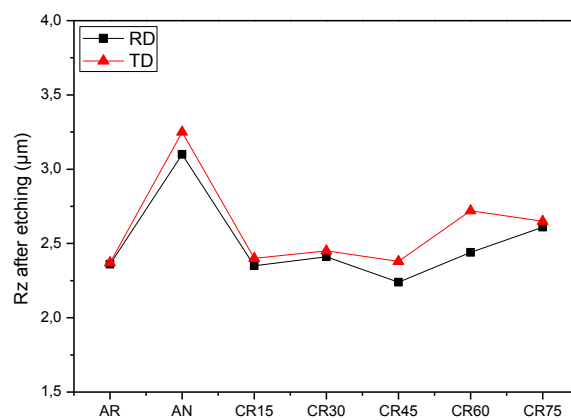


Figure 3.3 Rz values of rolling and transverse direction of etched samples.

Rz values of rolling direction and transverse direction of AR, AN, CR15, CR30, CR45, CR60, and CR75 are 2.36, 3.10, 2.35, 2.41, 2.24, 2.44, 2.61 μm , and 2.37, 3.25, 2.40, 2.45, 2.38, 2.72, 2.65 μm , respectively. When Figure 3.3 is compared with Figure 3.1, it is understood that polishing and etching decreased Rz values in rolling direction.

3.2 AFM Measurement Results

The effect of polishing and etching on surface roughness in nanoscale is investigated by AFM. Figure 3.4 shows Ra values of rolling and transverse directions of samples in nanoscale.

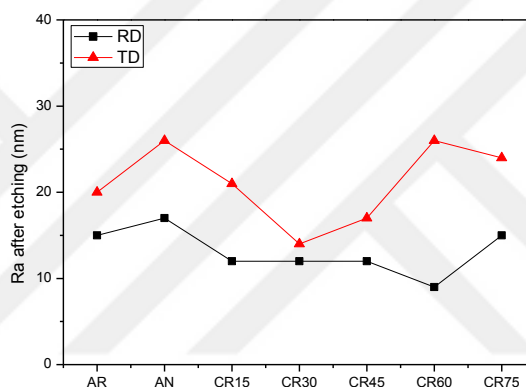


Figure 3.4 Ra values of samples in nanoscale.

Ra values of rolling direction and transverse direction of AR, AN, CR15, CR30, CR45, CR60, and CR75 are 15, 17, 12, 12, 12, 9, 15 nm, and 20, 26, 21, 14, 17, 26, 24 nm, respectively. Ra values of transverse direction are higher than that of rolling direction. Actually, Ra values of transverse and rolling directions of samples should be closer due to having the same polishing procedure. However, etching mechanisms were different because of grain orientation [60]. Figure 3.5 shows the schematic representation of etching mechanisms.

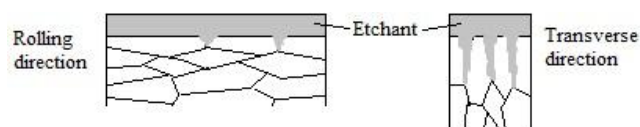


Figure 3.5 Schematic representation of etching mechanisms.

Grain boundaries are high energy regions due to instability. For this reason, etchant can penetrate to these regions easier than grain interior. This well known mechanism reveals the microstructure by selective corrosion of grain boundaries. As seen in Figure 3.5, etchant can easily penetrate up to another grain. Elongated grains block penetration of etchant in rolling direction; conversely, these grains simplify the penetration in transverse direction. Consequently, Ra values increased in transverse direction surface due to forming of big valleys. This mechanism can be seen in Rz values too. Figure 3.6 shows Rz values of rolling and transverse directions of samples in nanoscale.

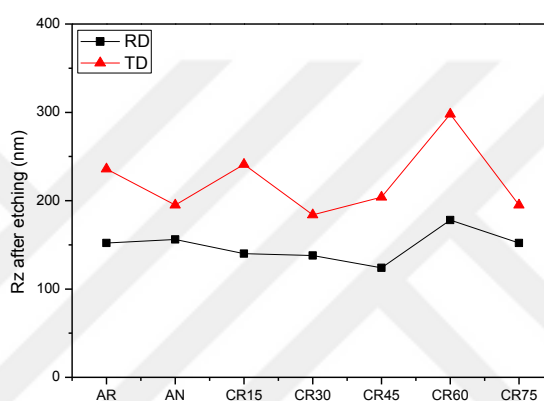


Figure 3.6 Rz values of samples in nanoscale.

Rz values of rolling direction and transverse direction of AR, AN, CR15, CR30, CR45, CR60, and CR75 are 152, 156, 140, 138, 124, 178, 152 nm, and 236, 195, 241, 184, 204, 298, 195 nm, respectively. Rz values of transverse direction are higher than that of rolling direction as expected. The reason is the same mechanism that seen in Ra values. The idea about different etching mechanisms due to grain orientation can be supported by three-dimensional surface topography images of samples. The red line on the scale bar symbolizes the mean value of surface roughness for each sample. In addition, the region that limited by gray lines below and above the red line represent the vast majority of measurements. There are maximum peak points above upper gray line, and minimum valley points below lower gray line. However, these points have little effect on the mean values. Topography image of rolling direction of AR is shown in Figure 3.7.

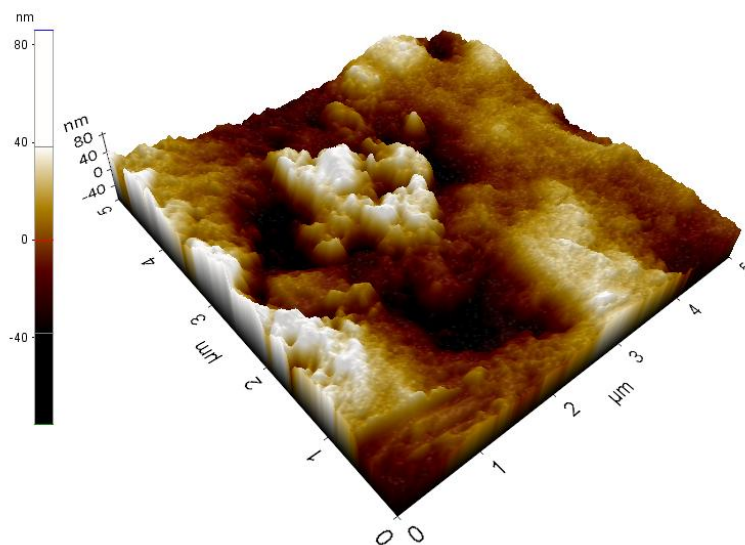


Figure 3.7 Topography image of rolling direction of AR.

As seen in Figure 3.7, white regions represent highest peaks, and black regions stand for deepest valleys. Roughness profiles of samples influenced by polishing and etching steps.

In addition, cold rolling reduction ratio increment affected the roughness profile by changing the grain orientation of samples. Figure 3.8 shows topography image of transverse direction of AR.

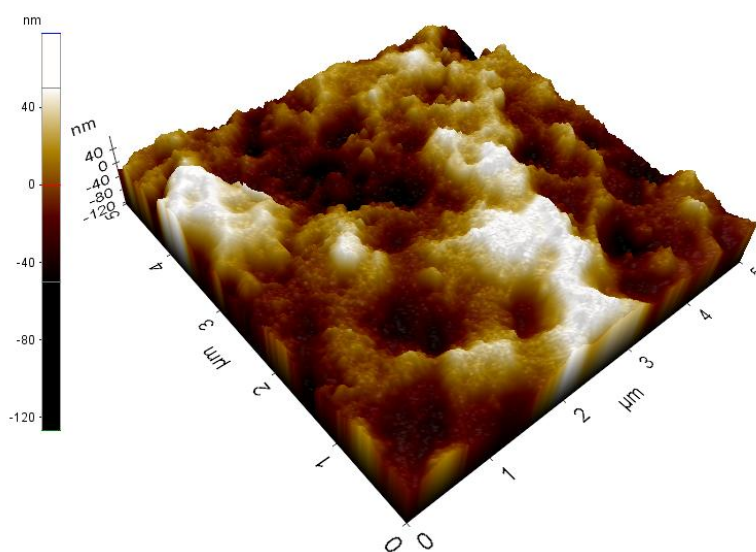


Figure 3.8 Topography image of transverse direction of AR.

As illustrated in Figure 3.8, the surface roughness of transverse direction of AR is more fluctuated in comparison with rolling direction of AR. Figure 3.9 shows topography image of rolling direction of AN.

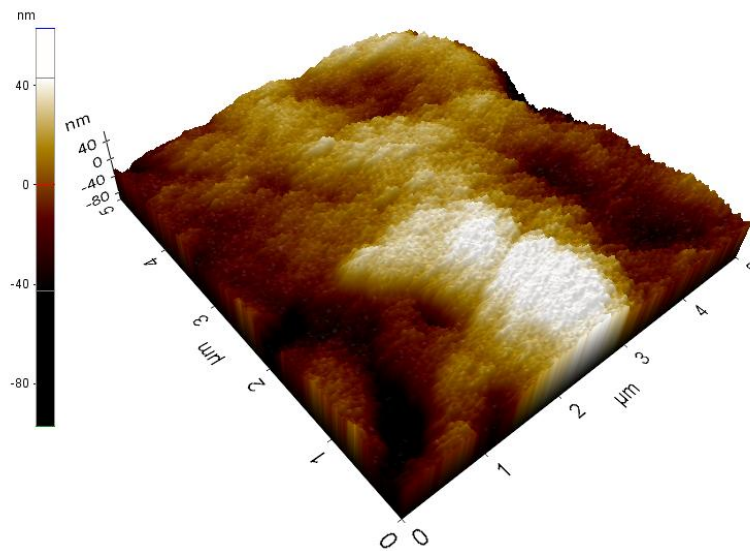


Figure 3.9 Topography image of rolling direction of AN.

As can be seen in Figure 3.9, the highest point is nearly 60 nm higher than mean value; on the other hand, the deepest point is almost 100 nm deeper than mean value. Topography image of transverse direction of AN is shown in Figure 3.10.

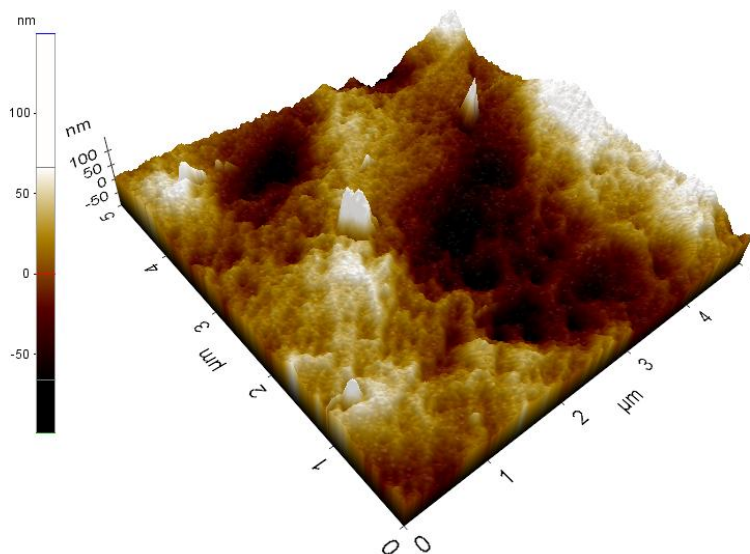


Figure 3.10 Topography image of transverse direction of AN.

As seen in Figure 3.10, distance between the highest peak and the deepest valley in transverse direction of AN is bigger than that in rolling direction of AN. Figure 3.11 shows topography image of rolling direction of CR15.

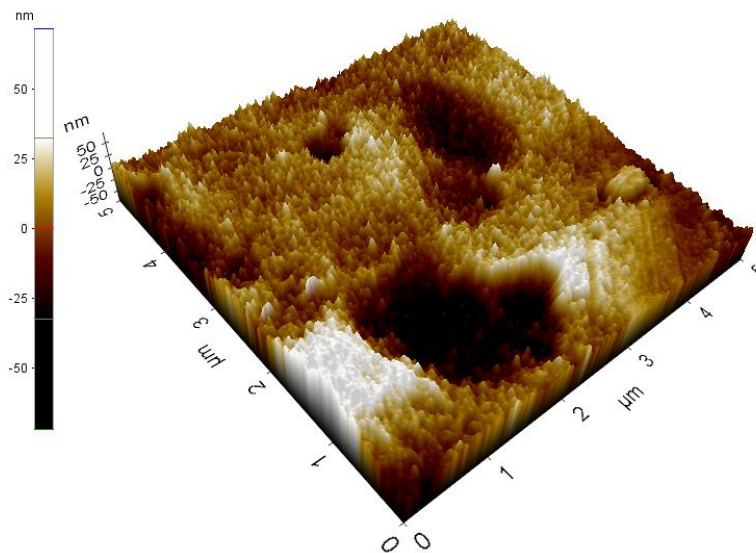


Figure 3.11 Topography image of rolling direction of CR15.

As illustrated in Figure 3.11, roughness profile changed with cold rolling when rolling direction of CR15 compared with rolling direction of AN. Figure 3.12 shows topography image of transverse direction of CR15.

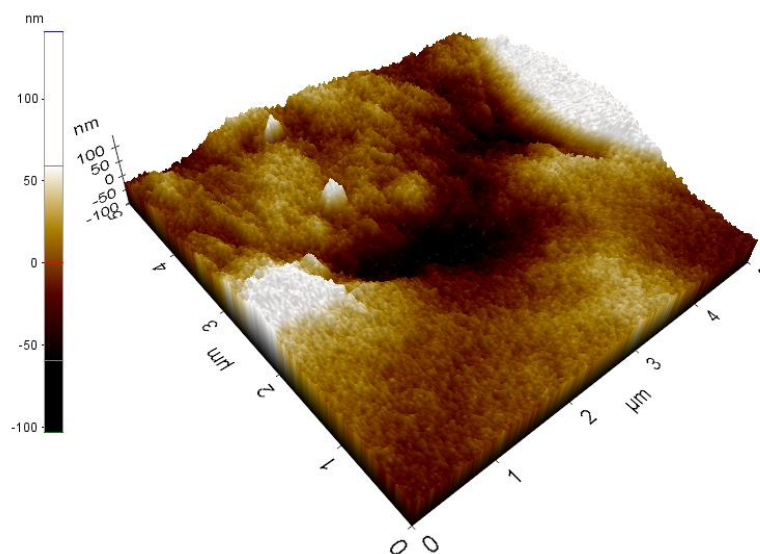


Figure 3.12 Topography image of transverse direction of CR15.

As seen in Figure 3.12, the vast majority of measurements are located between 60 and -60 according to the scale bar. Topography image of rolling direction of CR30 is shown in Figure 3.13.

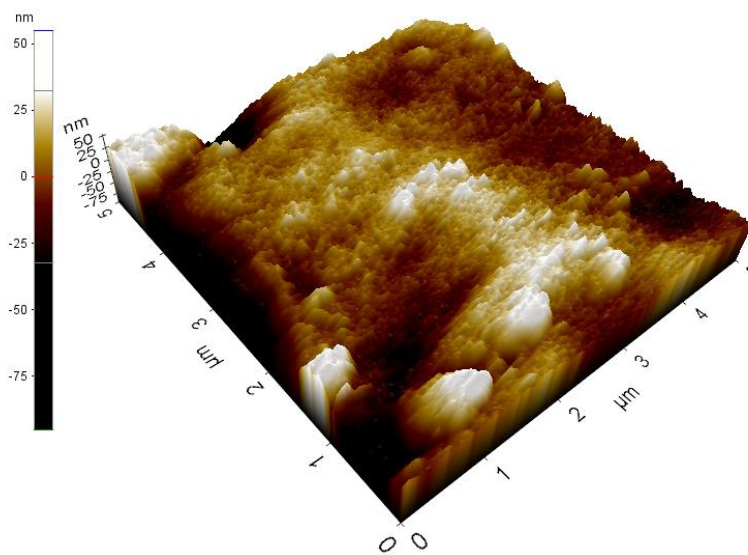


Figure 3.13 Topography image of rolling direction of CR30.

As can be seen in Figure 3.13, roughness profile continued to change with increasing of cold rolling reduction ratio. Figure 3.14 shows topography image of transverse direction of CR30.

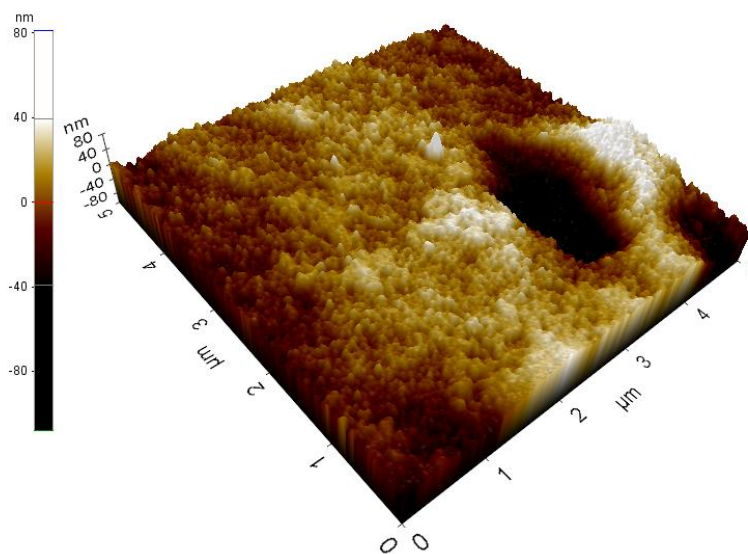


Figure 3.14 Topography image of transverse direction of CR30.

As seen in Figure 3.14, valleys of transverse direction are deeper than that of rolling direction. Figure 3.15 shows topography image of rolling direction of CR45.

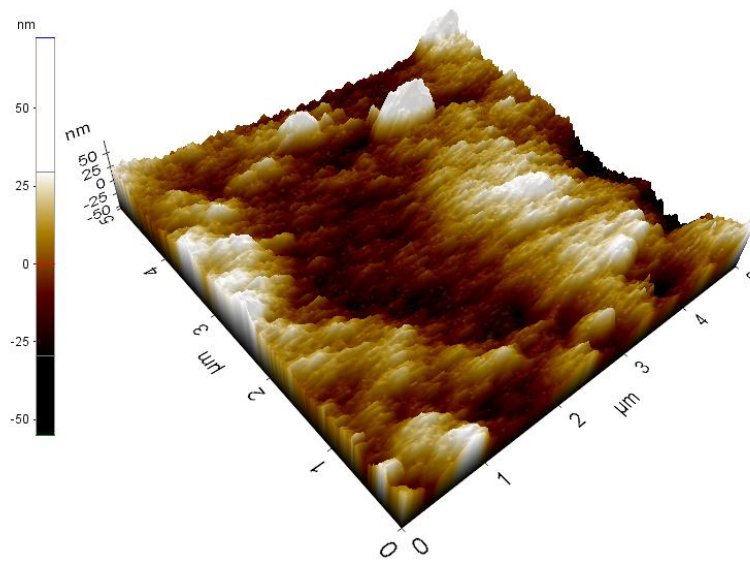


Figure 3.15 Topography image of rolling direction of CR45.

As illustrated in Figure 3.15, the vast majority of measurements are located approximately between 30 and -30. Topography image of transverse direction of CR45 is shown in Figure 3.16.

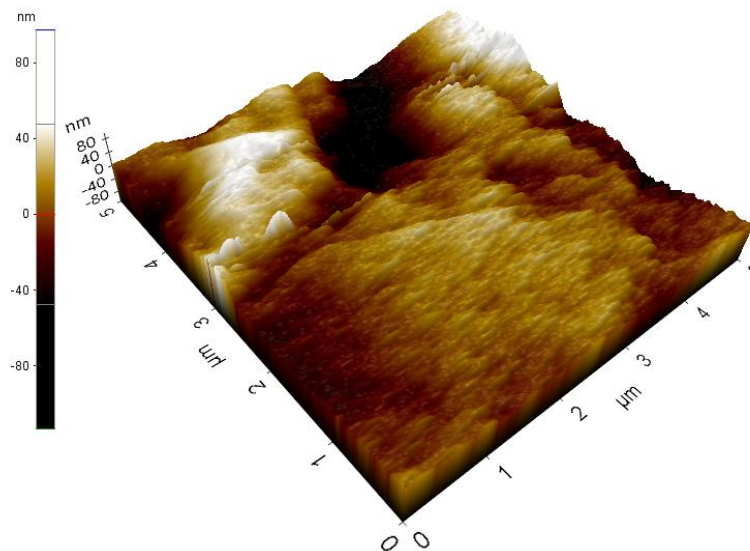


Figure 3.16 Topography image of transverse direction of CR45.

As can be seen in Figure 3.16, peaks are higher and valleys are deeper in comparison with Figure 3.15. Figure 3.17 shows topography image of rolling direction of CR60.

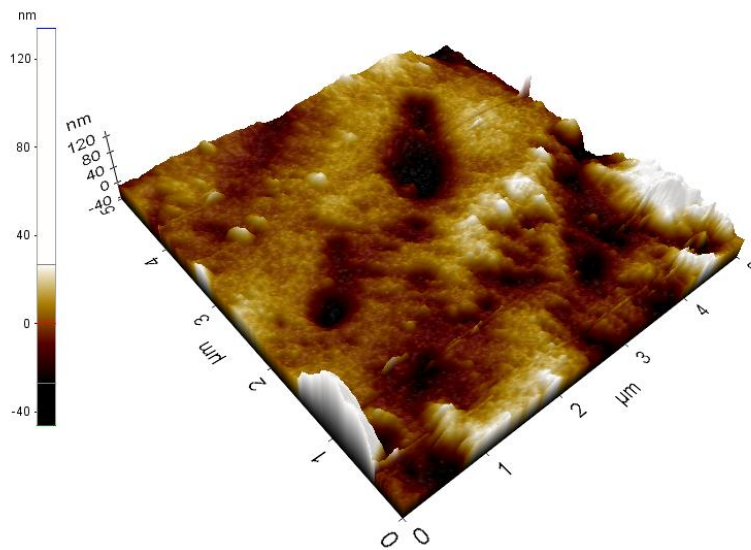


Figure 3.17 Topography image of rolling direction of CR60.

As illustrated in Figure 3.17, there are very high peak points in surface. They are approximately 140 nm higher than mean value. However, their effect on mean value is very little as can be seen from gray lines on the scale bar. Figure 3.18 shows topography image of transverse direction of CR60.

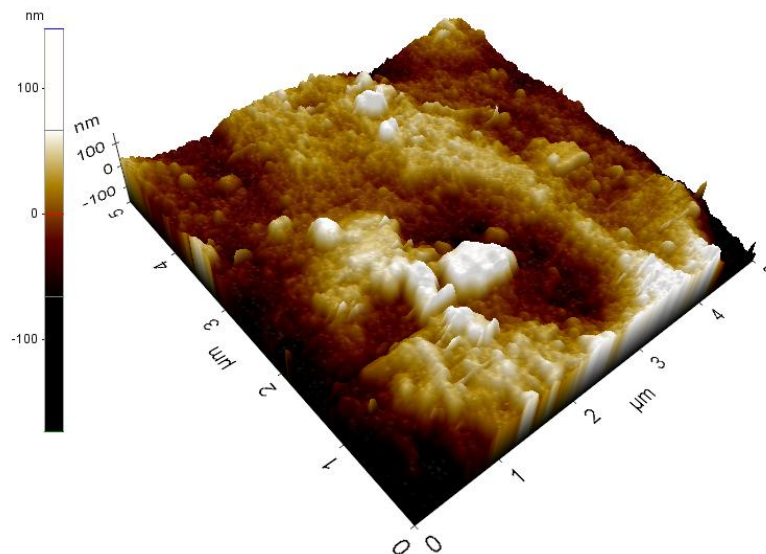


Figure 3.18 Topography image of transverse direction of CR60.

As seen in Figure 3.18, the vast majority of measurements are located nearly between 65 and -65. It is between 25 and -25 in rolling direction of same sample, so effect of etching mechanism can be seen clearly. Topography image of rolling direction of CR75 is shown in Figure 3.19.

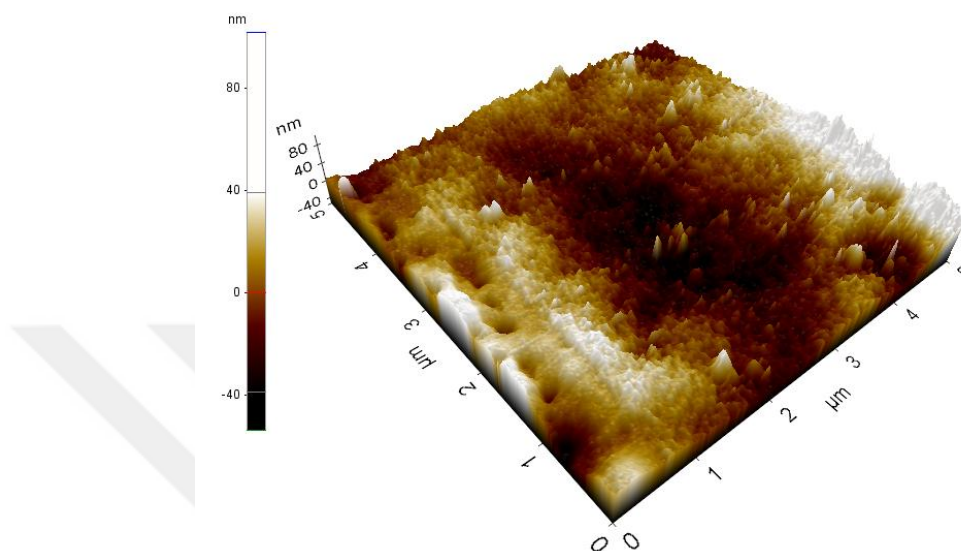


Figure 3.19 Topography image of rolling direction of CR75.

As seen in Figure 3.19, surface roughness profile of rolling direction of CR75 is in a good level. Figure 3.18 shows topography image of transverse direction of CR75.

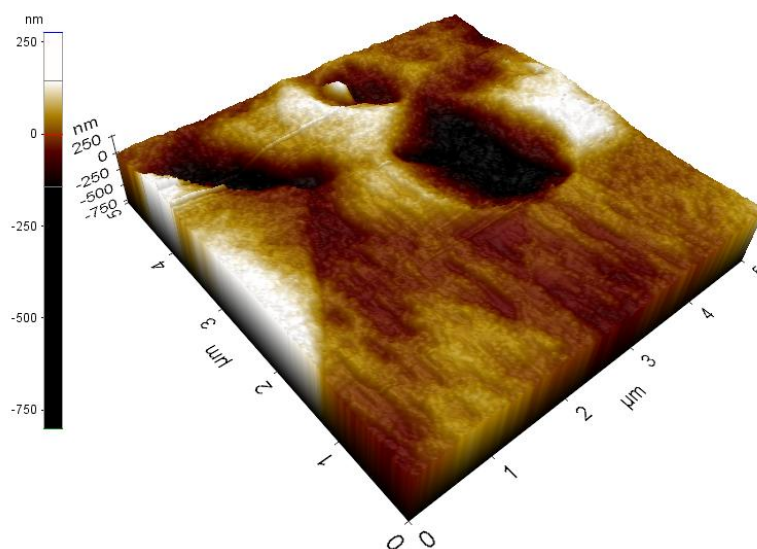


Figure 3.20 Topography image of transverse direction of CR75.

As illustrated in figures of topography images, peaks are higher and valleys are deeper in transverse directions of samples. This is the reason for high Ra and Rz values mentioned before in Figure 3.4 and Figure 3.6, respectively.

When the scale bars on the left side of topography images are analyzed, it can be seen that upper gray lines in topography images of transverse directions are higher than upper gray lines in topography images of rolling directions, and lower gray lines in topography images of transverse directions are lower than lower gray lines in topography images of rolling directions. In other words, the total quantity of peaks and valleys in transverse direction is higher than that of rolling direction. This situation demonstrates the idea about different etching mechanisms due to grain orientation that mentioned before in Figure 3.5.

3.3 Micro Vickers Hardness Tester Measurement Results

Microhardness test is performed both just after cold rolling process and after polishing and etching. The measurements after cold rolling illustrated the effect of cold rolling process on microhardness. On the other hand, micro Vickers hardness test after etching showed the effect of polishing and etching on microhardness. Figure 3.21 shows microhardness values of samples after cold rolling.

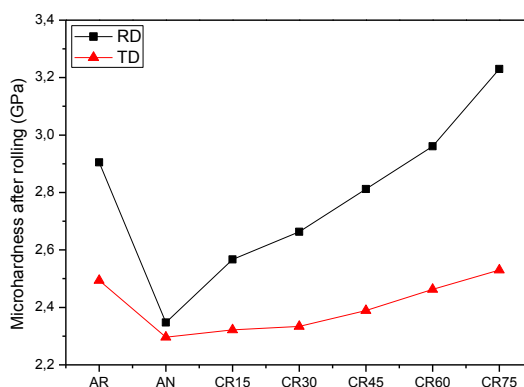


Figure 3.21 Microhardness values of samples after cold rolling.

Microhardness values of rolling and transverse direction of AR, AN, CR15, CR30, CR45, CR60, and CR75 after rolling are 2.905, 2.347, 2.567, 2.663, 2.812, 2.961, 3.230 GPa, and 2.494, 2.296, 2.322, 2.334, 2.389, 2.463, 2.530 GPa, respectively.

Microhardness value of samples increased with increasing cold rolling reduction ratio in both rolling and transverse directions. Grain refinement and work hardening are main mechanisms for microhardness increment [42]. It can be understood from Figure 3.21 that microhardness values of rolling direction of samples are higher than that of transverse direction of samples after cold rolling process. The reason for this is the grain orientation difference between two directions. The anisotropy of mechanical properties in materials with longitudinal grains is a well known fact [40].

It also can be seen in Figure 3.21 that the distance between microhardness value of rolling direction and microhardness value of transverse direction increased with increasing cold rolling reduction ratio. The evolution in grain refinement and work hardening mechanisms is the reason for increment in the distance between microhardness value of rolling direction and that of transverse direction. Work hardening mechanism in rolling direction is more effective than that in transverse direction, and its effect increases with increasing reduction ratio. On the other hand, grain refinement mechanisms in both directions are similar. The direction-dependent change of work hardening mechanism is the main factor for this situation [42]. Figure 3.22 shows microhardness values of samples after etching.

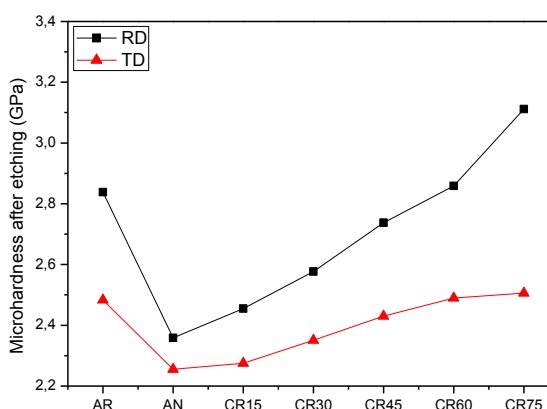


Figure 3.22 Microhardness values of samples after etching.

Microhardness values of rolling and transverse direction of AR, AN, CR15, CR30, CR45, CR60, and CR75 after etching are 2.838, 2.359, 2.455, 2.577, 2.738, 2.859, 3.112 GPa, and 2.483, 2.255, 2.275, 2.351, 2.43, 2.490, 2.506 GPa, respectively.

If Figure 3.21 and Figure 3.22 are analyzed together, it can be seen that polishing and etching have very little reducing effect on microhardness values of samples in both rolling and transverse directions. This situation reveals the relationship between surface roughness and hardness. As it is known, hardness increases with decreasing of surface roughness [61]. Etching slightly increased the surface roughness and thus reduced the hardness.

3.4 UMT Measurement Results

Nanoindentation results are represented by illustrating the graphs about the effect of multiple-stage loading profile (from 50 mN to 400 mN with 50 mN increase in each step) on depth of indentation mark. Figure 3.23 shows load-depth graphs of rolling and transverse directions of AR.

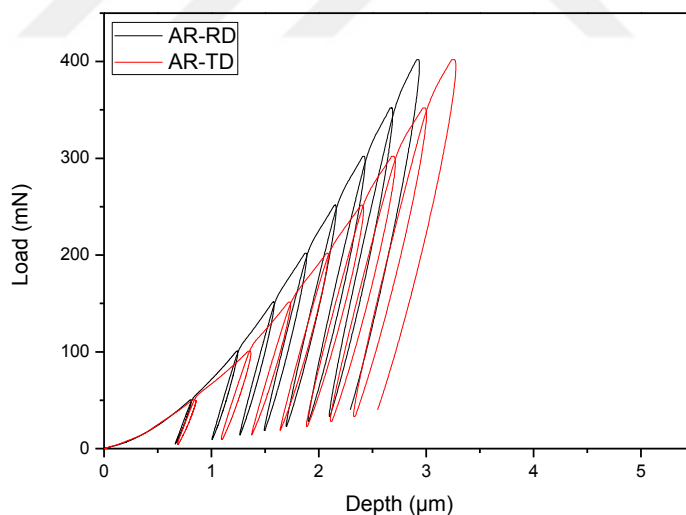


Figure 3.23 Load-depth graphs of rolling and transverse directions of AR.

As seen in Figure 3.23, the slope of load-depth curve of rolling direction is steeper than that of transverse direction. Steeper slope of the curve means higher elastic modulus. Furthermore, maximum depth value of transverse direction is higher than

that of rolling direction. Lower depth means higher hardness due to small projected area [62]. Consequently, elastic modulus and hardness values of rolling direction of AR are higher than that of transverse direction of AR. This result is in a good agreement with the information mentioned before in microhardness values. Figure 3.24 shows the load-depth graphs of rolling and transverse direction of AN.

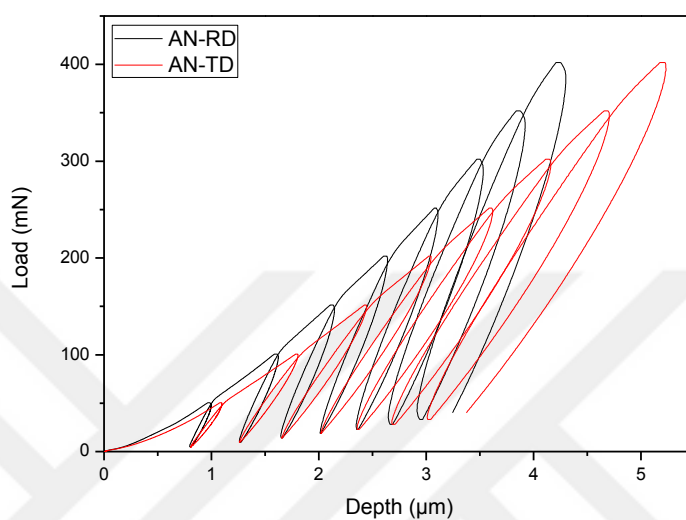


Figure 3.24 Load-depth graphs of rolling and transverse directions of AN.

As seen in Figure 3.24, the elastic modulus and hardness of rolling direction of AN are higher than that of transverse direction of AN. Figure 3.25 shows the load-depth graphs of rolling and transverse direction of CR15.

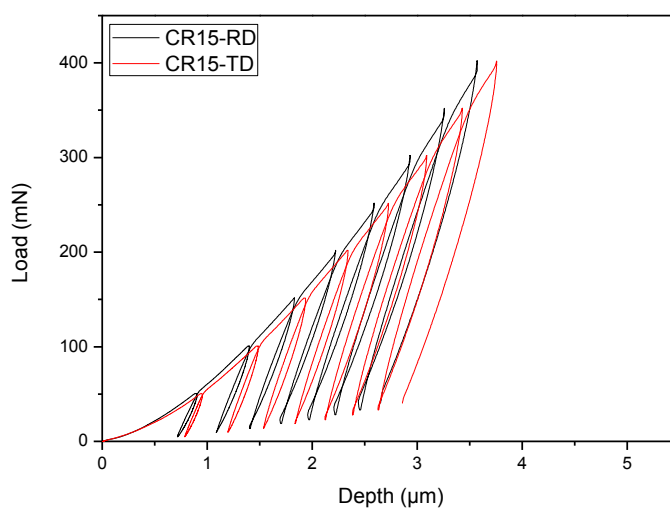


Figure 3.25 Load-depth graphs of rolling and transverse directions of CR15.

As can be seen in Figure 3.25, the difference in hardness and elastic modulus values of rolling direction and transverse direction of CR15 is similar to others. Figure 3.26 shows the load-depth graphs of rolling and transverse direction of CR30.

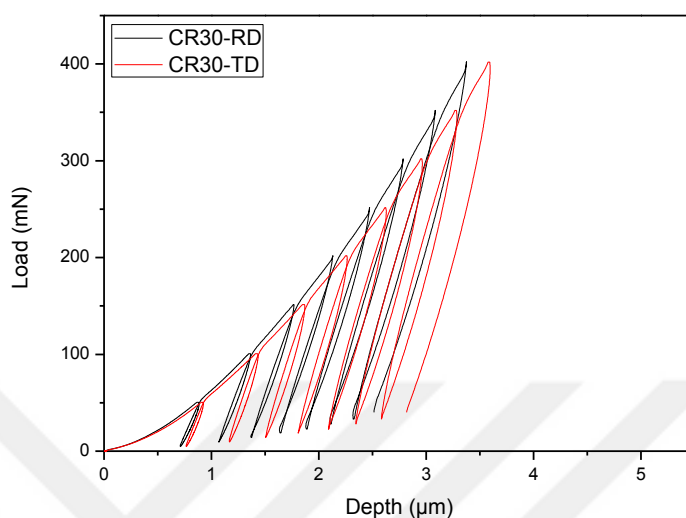


Figure 3.26 Load-depth graphs of rolling and transverse directions of CR30.

As seen in Figure 3.26, the slope of the curve is steeper, so the hardness and elastic modulus values are higher in rolling direction of CR30. Figure 3.27 shows the load-depth graphs of rolling and transverse direction of CR45.

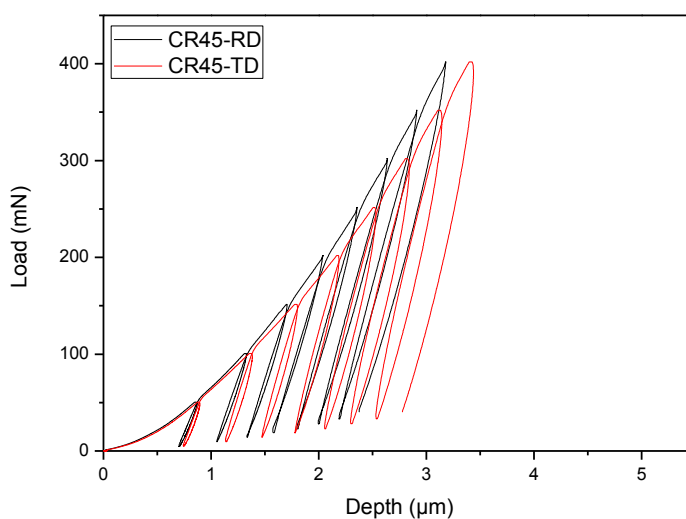


Figure 3.27 Load-depth graphs of rolling and transverse directions of CR45.

As seen in Figure 3.27, increment in hardness and elastic modulus due to steeper slope of the curve remains the same. In addition, curves are shifting to the left side with increasing cold rolling reduction ratio. Figure 3.28 shows the load-depth graphs of rolling and transverse direction of CR60.

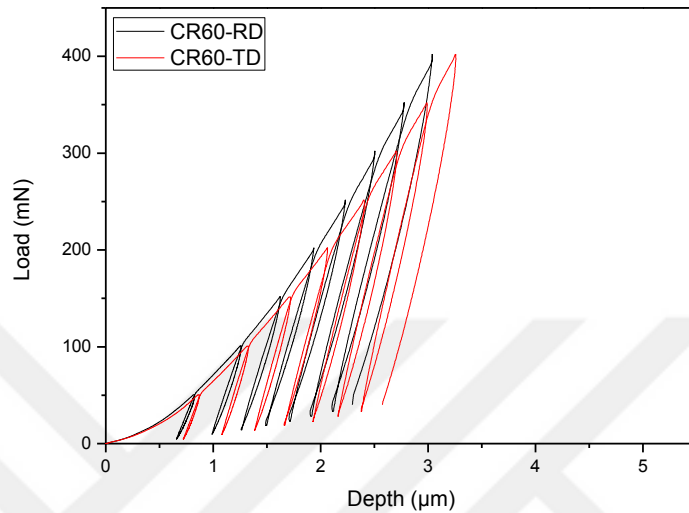


Figure 3.28 Load-depth graphs of rolling and transverse directions of CR60.

As seen in Figure 3.28, the difference in hardness and elastic modulus values of rolling direction and transverse direction of CR60 is very similar to AR. Figure 3.29 shows the load-depth graphs of rolling and transverse direction of CR75.

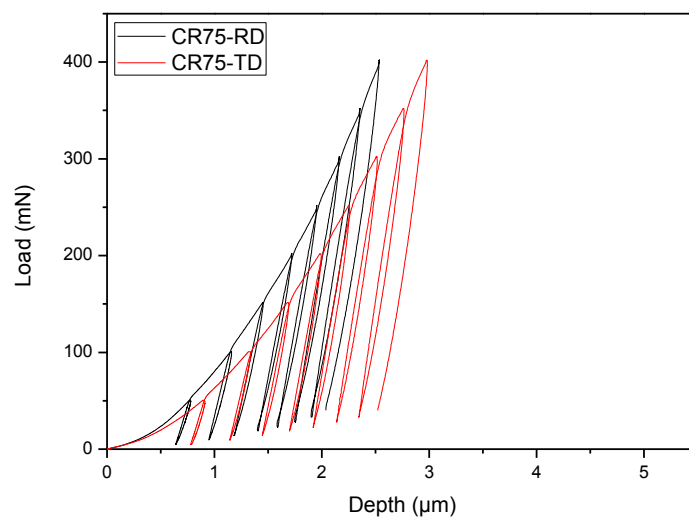


Figure 3.29 Load-depth graphs of rolling and transverse directions of CR75.

As seen in Figure 3.29, the shifting of the curves to the left side continued up to curves of CR75. CR75 has the highest elastic modulus and hardness values among other samples. Figure 3.30 shows load-depth graphs of rolling directions of samples.

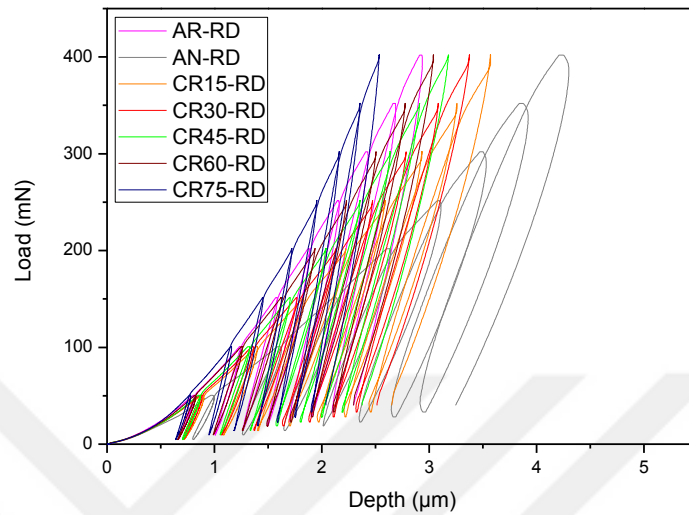


Figure 3.30 Load-depth graphs of rolling directions of samples.

As seen in Figure 3.30, CR75 has the highest hardness with minimum depth, and highest elastic modulus with steepest slope of curve. Conversely, AN has the lowest hardness and elastic modulus. Other samples took place according to their reduction ratios. Figure 3.30 shows load-depth graphs of transverse directions of samples.

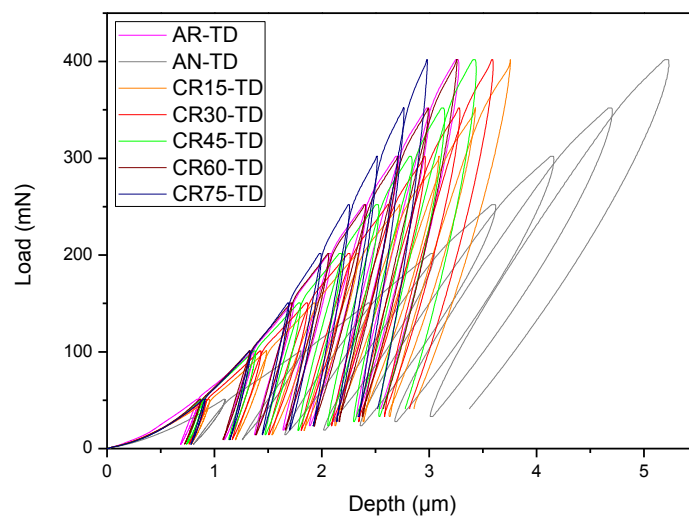


Figure 3.31 Load-depth graphs of transverse directions of samples.

As can be seen in Figure 3.31, the gradation of curves in transverse direction is similar to that in rolling direction. CR75 is the hardest sample with having the highest elastic modulus, and vice versa is valid for AN.

The homogeneity of samples can be explained with shape of the curves. If the curves of different loads (from 50 mN to 400 mN) form a regular line, it means that the sample is homogeneous. Load-depth figures of samples illustrate that the homogeneity of all samples are in a good level [63].

The nose of the curve is sharper in samples with high elastic modulus, and more cambered in samples with low elastic modulus. Internal stresses play an important role in this situation by influencing the recovery behavior [64]. Figure 3.32 shows average nanohardness values of samples after etching.

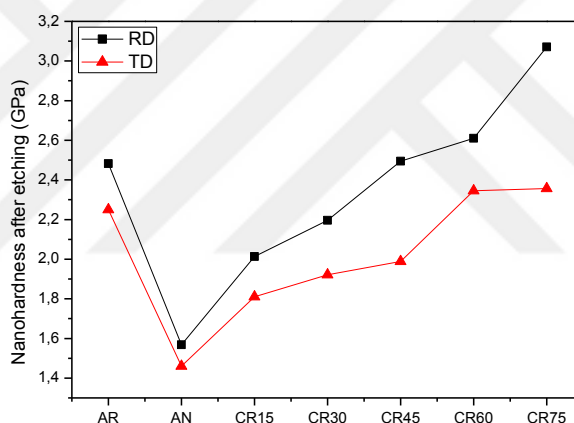


Figure 3.32 Average nanohardness values of samples after etching.

As seen in Figure 3.32, nanohardness increased with increasing of cold rolling reduction ratio as expected. Nanohardness values of rolling direction and transverse direction of AR, AN, CR15, CR30, CR45, CR60, and CR75 after etching are 2.482, 1.568, 2.013, 2.196, 2.494, 2.610, 3.071 GPa, and 2.250, 1.460, 1.810, 1.921, 1.989, 2.345, 2.356 GPa, respectively. Nanohardness values of AR in both directions are similar to those of CR60. Average nanohardness values of samples are in a good agreement with microhardness values and load-depth curves. Also, these values are in corroboration with the literature [65, 66]. Figure 3.33 shows the average elastic modulus values of samples.

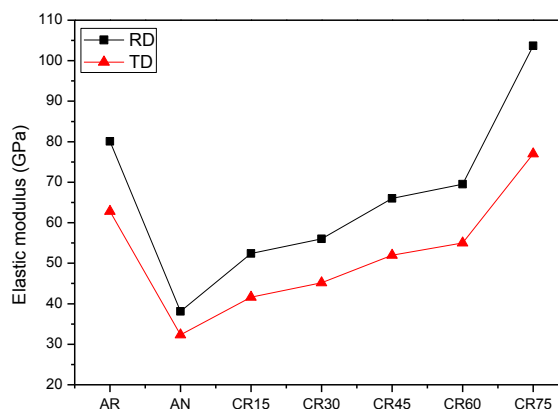


Figure 3.33 Average elastic modulus values of samples.

As can be seen in Figure 3.33, elastic modulus, nanohardness, and microhardness values are interrelated. Elastic modulus values of rolling direction and transverse direction of AR, AN, CR15, CR30, CR45, CR60, and CR75 are 80.1, 38.1, 52.4, 56, 66, 69.5, 103.7 GPa, and 62.8, 32.3, 41.6, 45.2, 52, 55, 77 GPa, respectively. Elastic modulus values increased with increasing reduction ratio. Moreover, elastic modulus values of AR are between CR60 and CR75.

3.5 Microstructural Analysis Results

Figure 3.34 shows the surface photographs of rolling direction of samples taken in 100X magnification just after cold rolling.

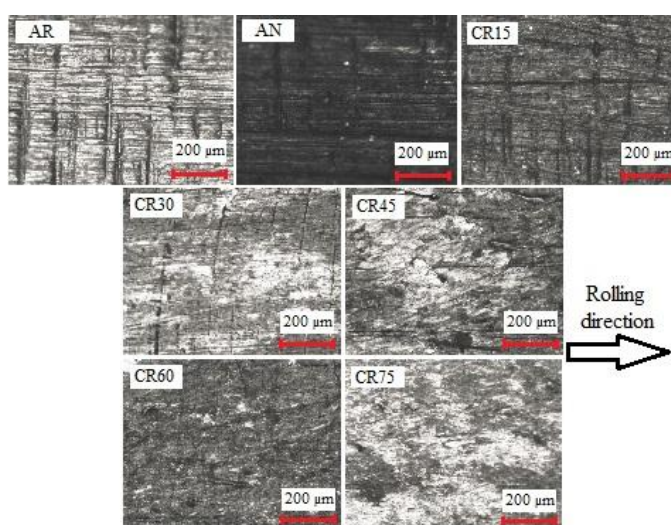


Figure 3.34 Surface photographs of rolling direction of samples.

As can be seen in Figure 3.34, AR has vertical cracks and horizontal deformation lines. These cracks and lines remained same after annealing and can be seen in AN. The effect of annealing on surface roughness could not be seen by naked eye in macroscale. However, the effect of cold rolling on surface roughness is very clear. Vertical cracks and horizontal deformation lines cleared away with increasing of cold rolling reduction ratio. In other words, cold rolling has a positive effect on surface roughness.

All samples are etched, and microstructure photographs are taken by inverted optical microscope in 1000X magnification to illustrate the grain structure, orientation, and size. Figure 3.35 shows microstructures of rolling and transverse directions of AR.

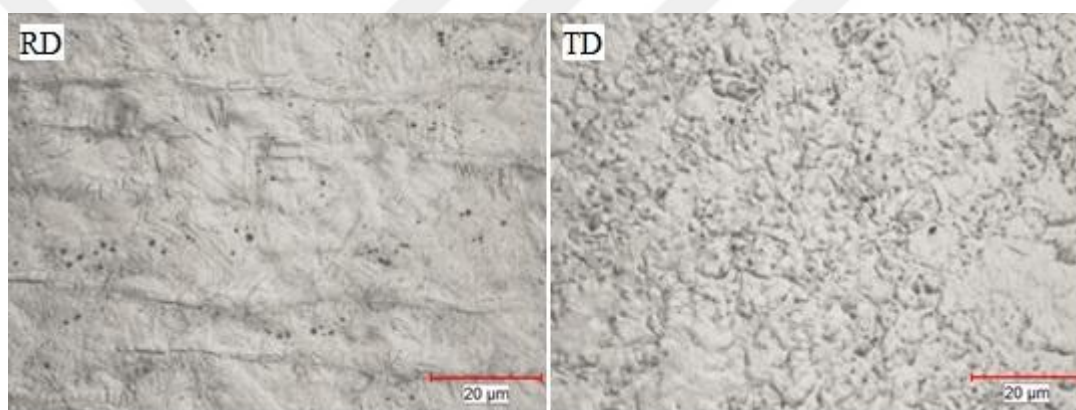


Figure 3.35 Microstructures of rolling and transverse directions of AR.

As seen in Figure 3.35, there are elongated and broken grains in rolling direction. Grain sizes are in the range of 5-15 μm . Rolling direction of sample has bigger grains due to elongation derived from cold rolling. Furthermore, there are some overlong grains in rolling direction. These overlong grains are not typical for cold rolled materials, and can be seen in hot rolled samples.

As mentioned before, production route for rod shaped materials includes hot extrusion, multiple cold rolling, and annealing. The overlong grains should be derived from the hot rolling part of production route. Figure 3.36 shows microstructures of rolling and transverse directions of AN.

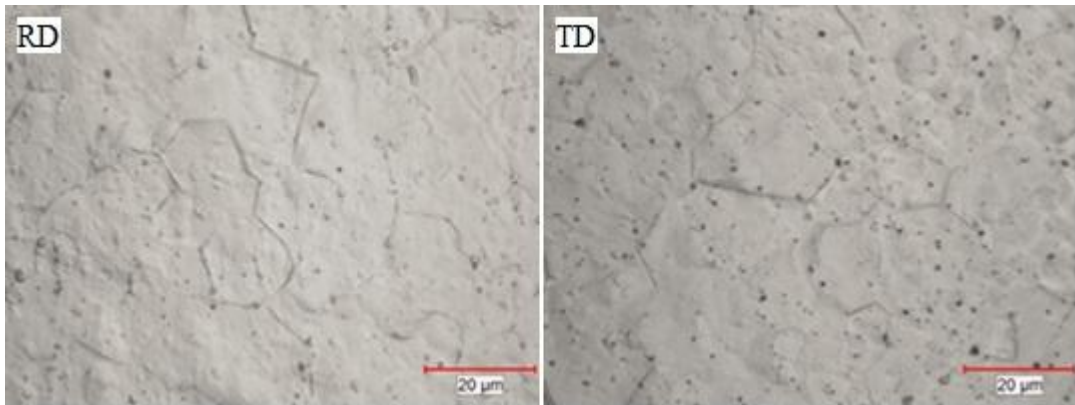


Figure 3.36 Microstructures of rolling and transverse directions of AN.

As illustrated in Figure 3.36, there are equiaxed big grains in both rolling and transverse direction. Grain sizes are in the range of 10-25 μm . Black points on the surface are defects and voids. The orientation could not be seen due to absence of cold rolling process. Figure 3.37 shows microstructures of rolling and transverse directions of CR15.

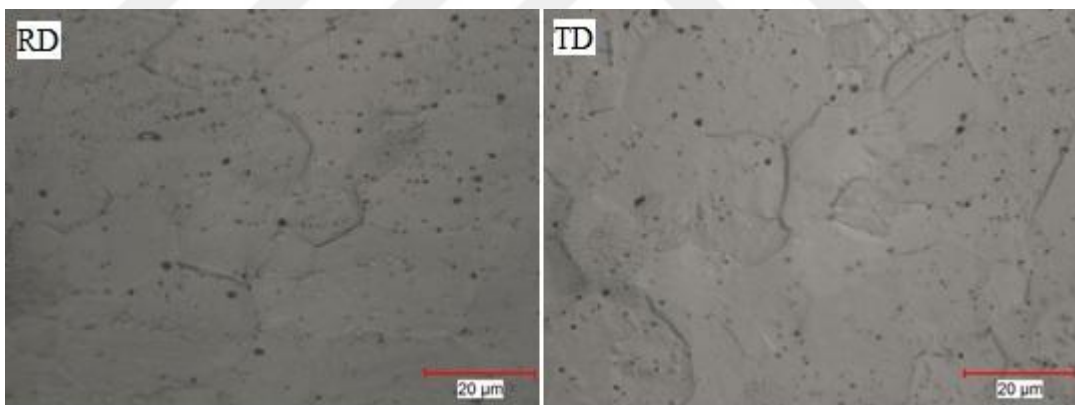


Figure 3.37 Microstructures of rolling and transverse directions of CR15.

As seen in Figure 3.37, the difference between AN and CR15 is very little. The most notably difference is the alignment of some voids in the rolling direction. In addition, grain size is slightly lower than AN in both directions. Figure 3.38 shows microstructures of rolling and transverse directions of CR30.

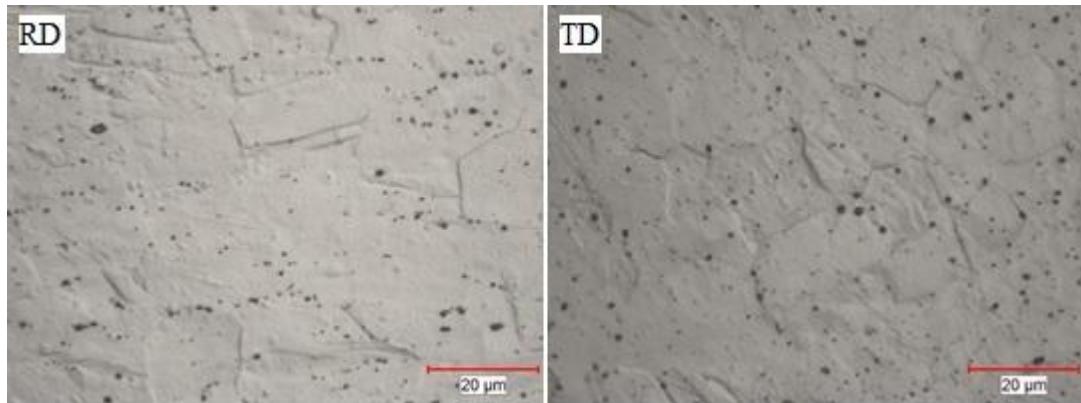


Figure 3.38 Microstructures of rolling and transverse directions of CR30.

As can be seen in Figure 3.38, grains started to elongate in rolling direction, while getting smaller in transverse direction. Grain boundary orientation started to form along the rolling direction. Grain sizes are in the range of 12-20 μm. Figure 3.39 shows microstructures of rolling and transverse directions of CR45.

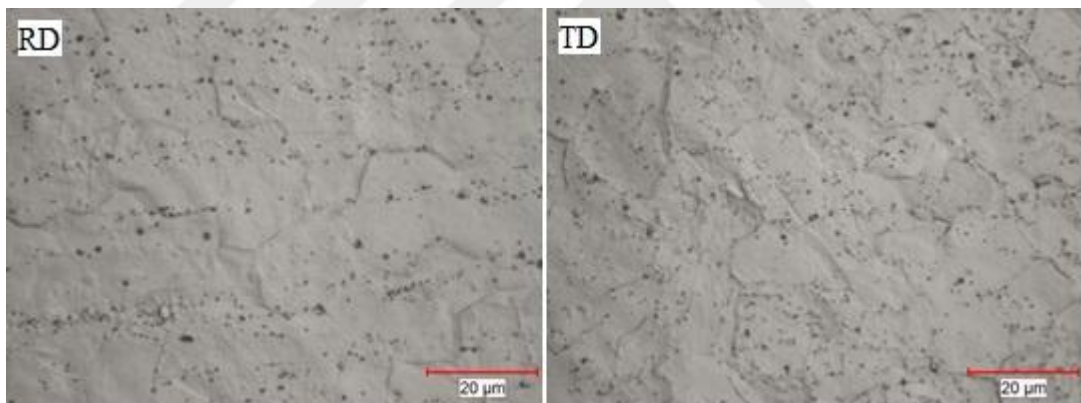


Figure 3.39 Microstructures of rolling and transverse directions of CR45.

As illustrated in Figure 3.39, grain boundary orientation and alignment of voids started to create a band structure in rolling direction. Grains in rolling and transverse directions are smaller than that of CR30. The grain size range is nearly 10-15. The grain sizes in transverse direction are slightly lower than those of rolling direction. Figure 3.40 shows microstructures of rolling and transverse directions of CR60.

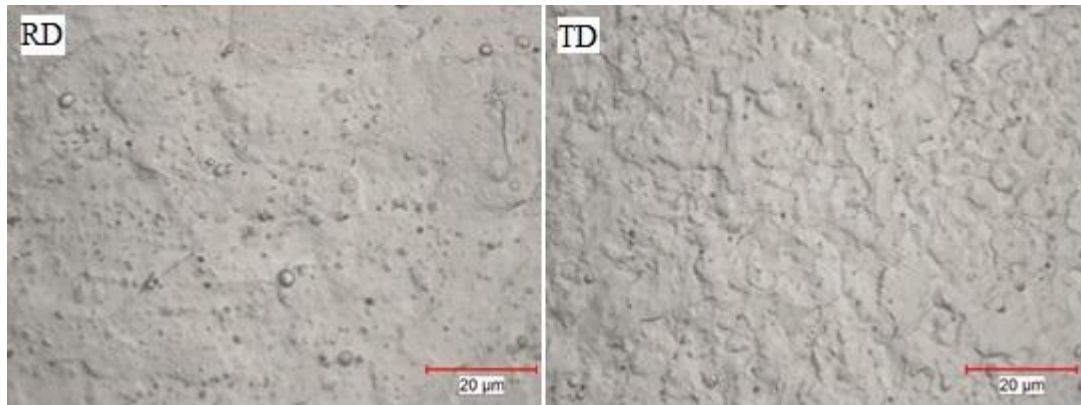


Figure 3.40 Microstructures of rolling and transverse directions of CR60.

As seen in Figure 3.40, grain sizes of rolling and transverse directions continue to decreasing. Grain sizes of CR60 are in the range of 5-13. Figure 3.41 shows microstructures of rolling and transverse directions of CR75.

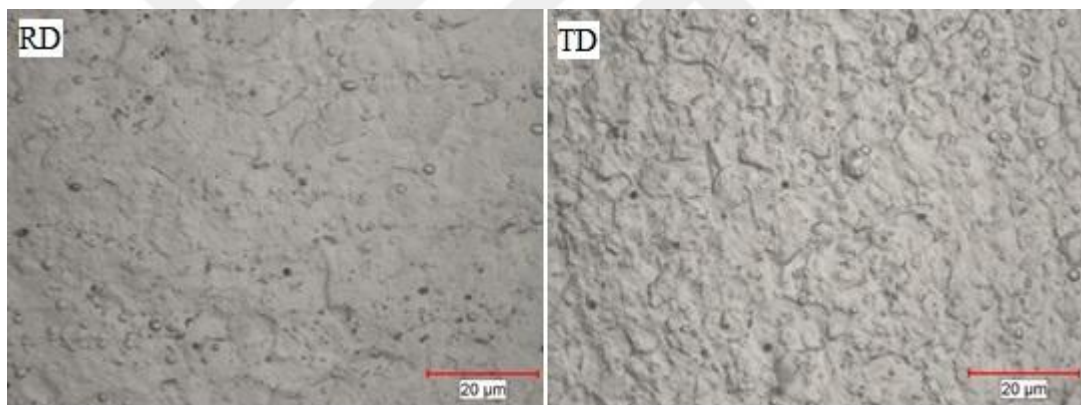


Figure 3.41 Microstructures of rolling and transverse directions of CR75.

As illustrated in Figure 3.41, an orientation formed along the rolling direction. Grain sizes in rolling and transverse directions reached to their minimum values in the range of 3-10. Transverse direction of CR75 has lower grain sizes than rolling direction like other samples.

The hardness increased with decreasing of grain size in rolling direction. For example, CR75-RD is harder than CR60-RD by having smaller grains. On the other hand, CR75-RD is harder than CR75-TD but grains of CR75-TD are smaller.

As mentioned before, the mechanisms for increasing of hardness are grain refinement and work hardening. The work hardening mechanism is more effective in rolling direction. In addition, the anisotropy due to grain orientation affects the hardness. The effects of work hardening and grain orientation are more dominant than grain refinement effect. Consequently, higher hardness of CR75-RD from CR75-TD becomes reasonable, although grains of CR75-RD are bigger. Figure 3.42 shows average grain sizes of samples.

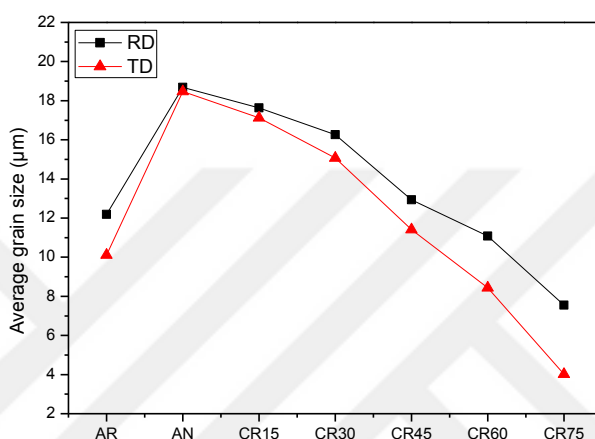


Figure 3.42 Average grain sizes of samples.

Average grain sizes of rolling direction and transverse direction of AR, AN, CR15, CR30, CR45, CR60, and CR75 are 12.19, 18.68, 17.63, 16.26, 12.93, 11.08, 7.55 μm, and 10.11, 18.47, 17.12, 15.07, 11.41, 8.43, 4.02 μm, respectively. As seen in Figure 3.42, average grain sizes of transverse directions are lower than average grain sizes of rolling directions. In addition, average grain size decreased with increasing of cold rolling reduction ratio. Average grain size values of AR are between CR45 and CR60.

3.6 Elemental Analysis Results

The quantity of alloying elements is investigated by elemental analysis. Measurements are evaluated from fracture surfaces of samples in 10000X magnification. Figure 3.43 shows the SEM photograph taken in 10000X magnification and the graph of EDS result for CR45.

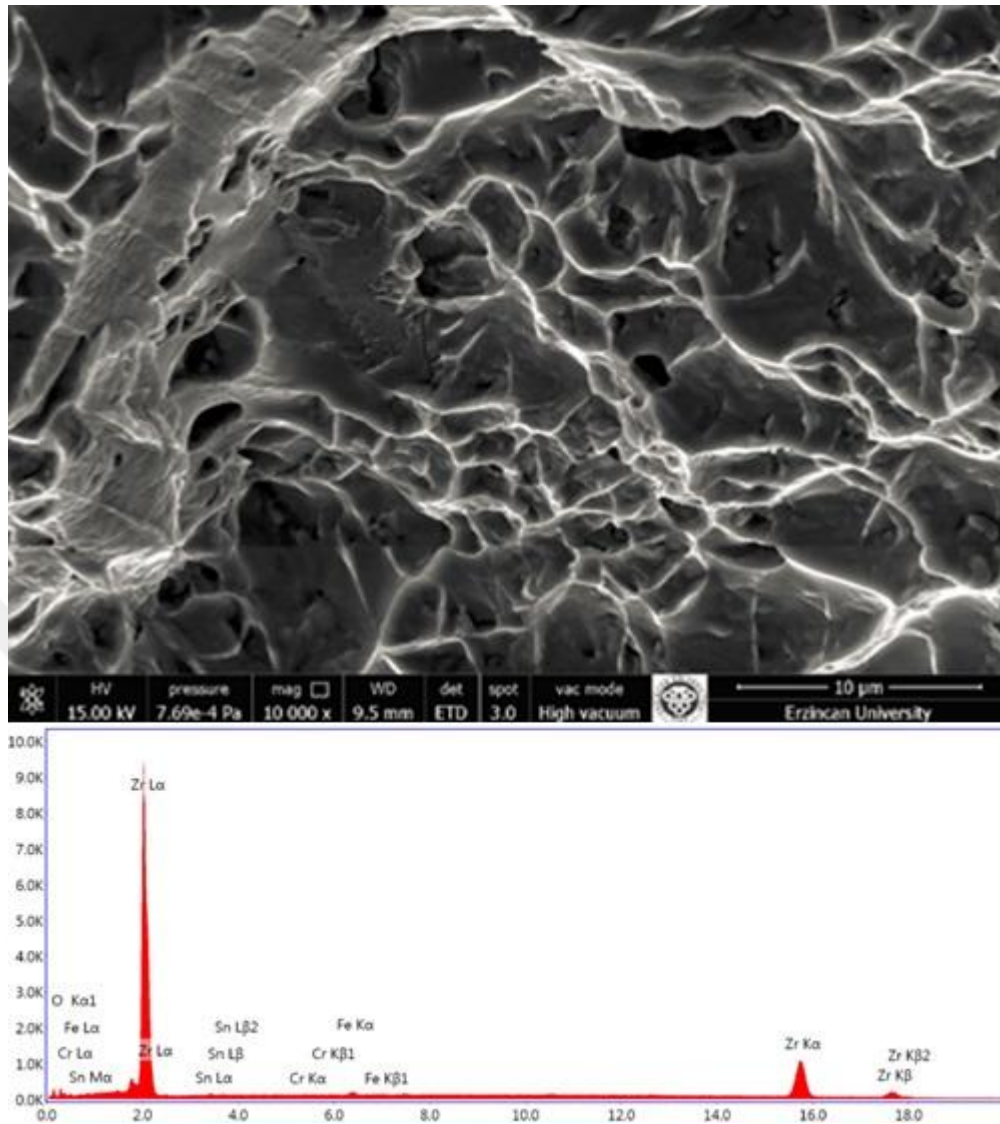


Figure 3.43 SEM photograph (up) and graph of EDS result (down) for CR45.

As seen in Figure 3.43, there are only alloying elements in structure. Consequently, rolling and annealing processes did not cause any contamination. EDS result represents entire SEM photograph to see the general distribution of alloying elements. Graphs of EDS results for other samples are nearly same with CR45, so only CR45 is represented. SEM photographs of other samples will be illustrated in fractography study results.

The weight percentage of each alloying element is illustrated by elemental analysis. Table 3.1 shows elemental analysis results of samples.

Table 3.1 Elemental analysis results of samples.

	wt % Zr	wt % Sn	wt % Cr	wt % Fe	wt % O
AR	91.66±1.00	0.97±0.46	0.19±0.11	0.95±0.23	6.23±1.90
AN	87.74±0.90	0.85±0.38	0.16±0.09	1.01±0.19	10.24±1.92
CR15	86.17±0.90	0.81±0.39	0.21±0.12	0.75±0.21	12.06±2.15
CR30	89.38±1.00	0.87±0.44	0.16±0.09	0.95±0.25	8.65±1.80
CR45	89.30±1.00	0.60±0.36	0.12±0.07	0.97±0.22	9.01±1.99
CR60	91.43±0.99	0.64±0.38	0.18±0.10	0.86±0.21	6.88±1.92
CR75	90.99±1.28	1.18±0.51	0.24±0.14	0.89±0.29	6.70±1.20
Procured	97.77	1.70	0.13	0.24	0.16

As can be seen in Table 3.1, contents of Sn, Cr, and Fe are very close for each sample. The point of interest is the weight percentages of O. The weight percentage of O in starting material was 0.16, so a large quantity of O is absorbed by each sample.

The first reason for high O content is storage conditions. No protective measure is applied to samples during storage. The second reason is high surface area due to high surface roughness derived from fracture. O absorption probability increases with increasing of surface area [67]. It is normal that, O absorption will start from the surface of sample. As a result, weight percentage of O on surface can be higher than whole sample. High O content in AR can be explained by these reasons, but the situation is somewhat different for other samples.

AN, CR15, CR30, CR45, CR60, and CR75 are annealed in controlled atmosphere as mentioned before. Samples might be absorbed O due to low quality of furnace or human errors. It is known from surface measurement results that surface roughness value of AN is the highest one. Therefore, the higher O content of AN from AR becomes reasonable. Cold rolling process should be taken into consideration while explaining the O contents of CR15, CR30, CR45, CR60, and CR75. Cold rolling process consists of rolling and heating steps. Each step has different effects on O absorption of samples. Heating steps are performed in a simple heat treatment furnace in air atmosphere at 300°C.

First heating step is examined to CR15, CR30, CR45, CR60, and CR75 samples for 30 minutes. Then, other heating steps are performed before each pass for 5 minutes. Consequently, heating step quantities for CR15, CR30, CR45, CR60, and CR75 are 1, 2, 3, 4, and 5, respectively. In addition, total heating times for each sample are 30, 35, 40, 45, and 50 minutes, respectively. As a result, O should be absorbed by cold rolled samples in heating steps due to uncontrolled atmosphere and high temperature.

Another step of cold rolling process is the rolling step. The surface roughness decreases with increasing of reduction ratio as mentioned before. The relation between surface roughness and O absorption in Zircaloy-4 is investigated by many researchers, and it is found that O absorption increased with increasing surface roughness [67-69]. Consequently, O absorption decreased with increasing cold rolling reduction ratio.

As can be seen in Table 3.1, O content is in a decreasing tendency from CR15 to CR75. There are two mechanisms about O absorption in cold rolled samples. The mechanism in heating step has an absorption increasing effect while that in rolling step has an absorption decreasing effect.

Since there is a decreasing tendency of O content from CR15 to CR75, it can be deduced that the mechanism in rolling step is more dominant than that in heating step.

3.7 Phase Analysis Results

Phase analysis results are represented by intensity values for 2-theta degrees between 30° and 85°. Intensity peaks of samples are compared with the characteristic peaks of Zr- α [70]. Figure 3.44 shows the characteristic peaks of Zr- α phase measured with Cu anode material.

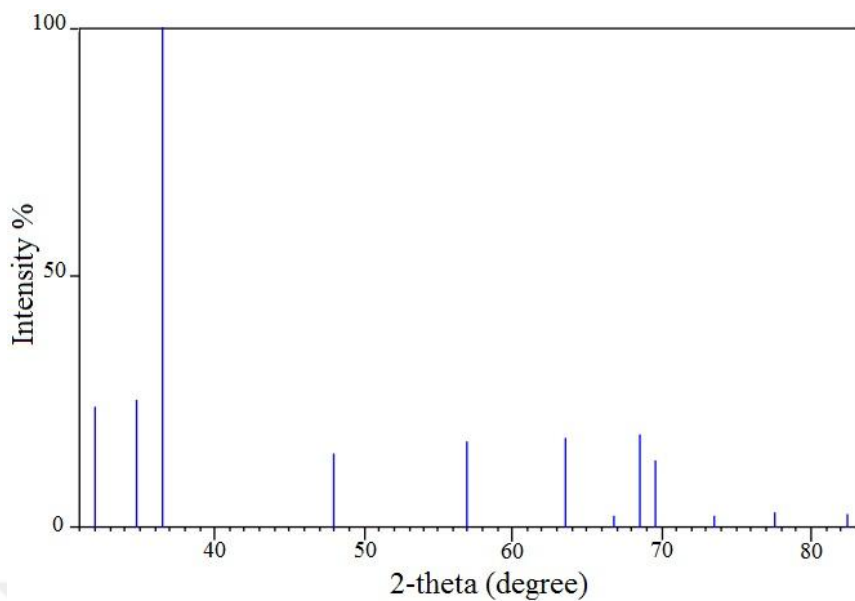


Figure 3.44 Characteristic XRD peaks of Zr- α .

As seen in Figure 3.44, Zr- α has 12 peaks in the positions of 31.9°, 34.8°, 36.5°, 47.9°, 56.9°, 63.5°, 66.8°, 68.5°, 69.5°, 73.5°, 77.5°, and 82.4° with different intensity percentages. Figure 3.45 shows XRD peaks of samples.

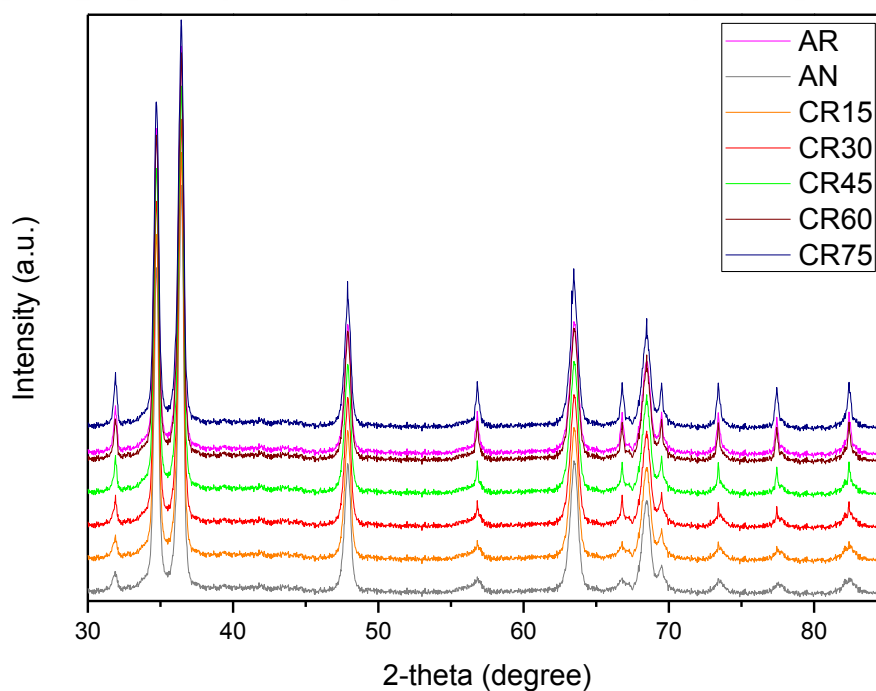


Figure 3.45 XRD peaks of samples.

As seen in Figure 3.45, peaks are shifted to up side with increasing of cold rolling reduction ratio. This situation is in a good agreement with literature [41, 64]. In addition, there are only characteristic peaks of Zr- α . It means that, there is only Zr- α phase in structure. On the other hand, the formation of an oxide phase can be questioned due to very high content of oxygen in samples. However, a large quantity of O can dissolve in interstitial positions of Zr- α without changing properties at temperatures between 25°C and 350°C [71]. For this reason, the absence of oxide phase can be explained by this way.

3.8 Fractography Study Results

Fracture surface pictures of samples are taken randomly in 1000X and 5000X magnification with high vacuum mode to illustrate fracture behavior of samples. Figure 3.46 shows fractography images of AR in 1000X and 5000X magnification.

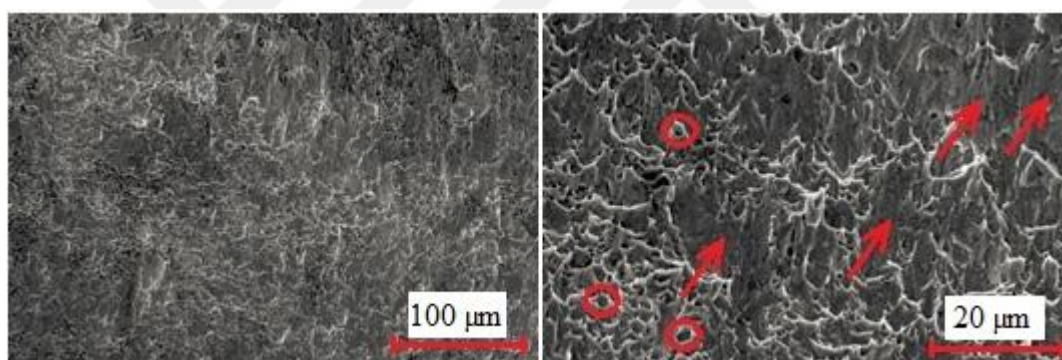


Figure 3.46 Fractography images of AR in 1000X (left) & 5000X (right).

Flat areas shown with arrows represent the quasi-cleavage surfaces; on the other hand, small voids shown with circles stand for dimples. Cleavage surfaces are characteristic for brittle materials, and dimples are characteristic for ductile materials. Furthermore, cleavage surfaces and dimples can be located together in most of the metals, and this situation is named mixed fracture mode [72, 73].

As seen in Figure 3.46, the amount of quasi-cleavage surfaces is higher than amount of dimples. Consequently, the fracture behavior is mixed fracture mode but it is

closer to brittle fracture mode more than ductile fracture mode. Figure 3.47 shows fractography images of AN in 1000X and 5000X magnification.

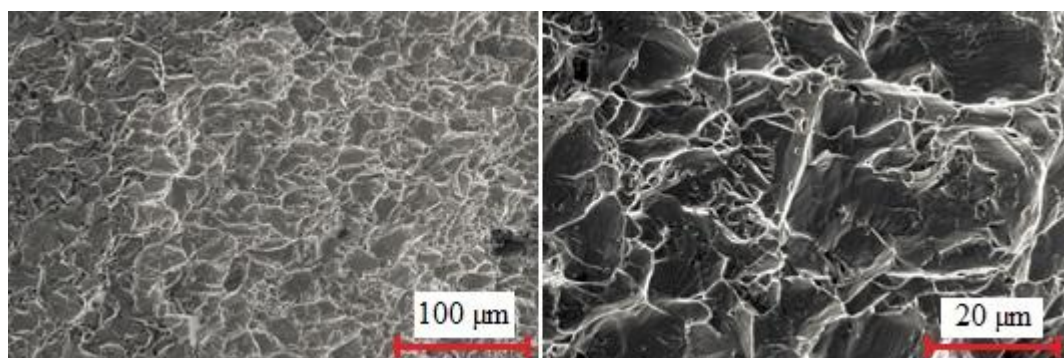


Figure 3.47 Fractography images of AN in 1000X (left) & 5000X (right).

As can be seen in Figure 3.47, there are a lot of big dimples and little quasi-cleavage surfaces, so the fracture behavior is mixed fracture mode but closer to ductile fracture mode. Figure 3.48 shows fractography images of CR15 in 1000X and 5000X magnification.

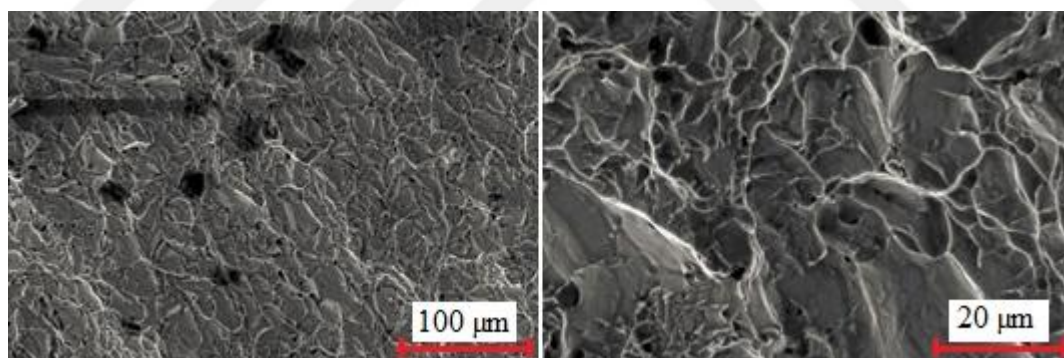


Figure 3.48 Fractography images of CR15 in 1000X (left) & 5000X (right).

As seen in Figure 3.48, the amount of dimples decreased and quasi-cleavage surfaces increased slightly in comparison with AN. There are big cavities in the fractography image taken in 1000X. These cavities assumed to be voids that formed in fabrication process, because they too big to consider like a dimple. Figure 3.49 shows fractography images of CR30 in 1000X and 5000X magnification.

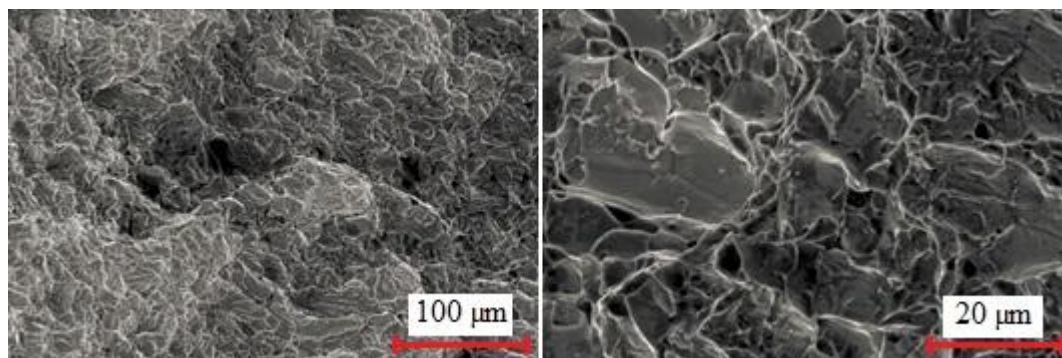


Figure 3.49 Fractography images of CR30 in 1000X (left) & 5000X (right).

As illustrated in Figure 3.49, the amount of dimples continued to decrease and quasi-cleavage surfaces became more dominant when compared with CR15. The elastic modulus and hardness increased with increasing of cold rolling reduction ratio as mentioned before. Therefore, mixed fracture mode became closer to brittle fracture mode. Figure 3.50 shows fractography images of CR45 in 1000X and 5000X magnification.

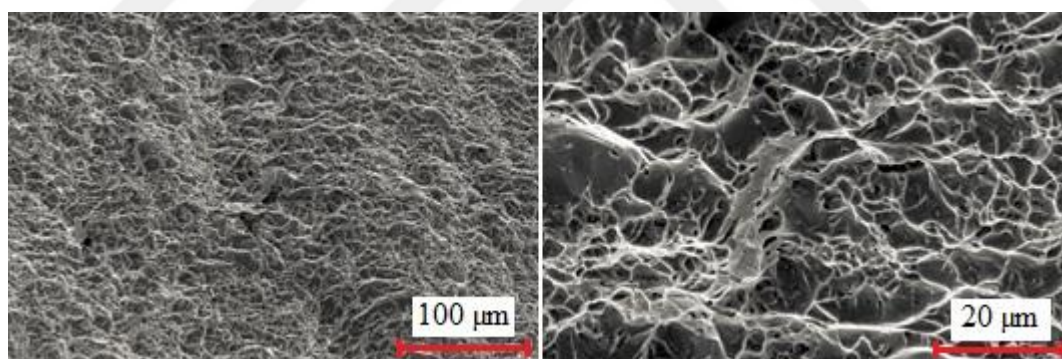


Figure 3.50 Fractography images of CR45 in 1000X (left) & 5000X (right).

As seen in Figure 3.50, there is an obvious superiority of quasi-cleavage surfaces on dimples. This situation is related with high elastic modulus and hardness. In addition, the surface roughness of samples can be illustrated by fractography images taken in 5000X magnification. It is obvious that roughness profile of fractography images decreased with increasing of cold rolling reduction ratio. These images are in a good agreement with microscale and nanoscale surface roughness results. Figure 3.51 shows fractography images of CR60 in 1000X and 5000X magnification.

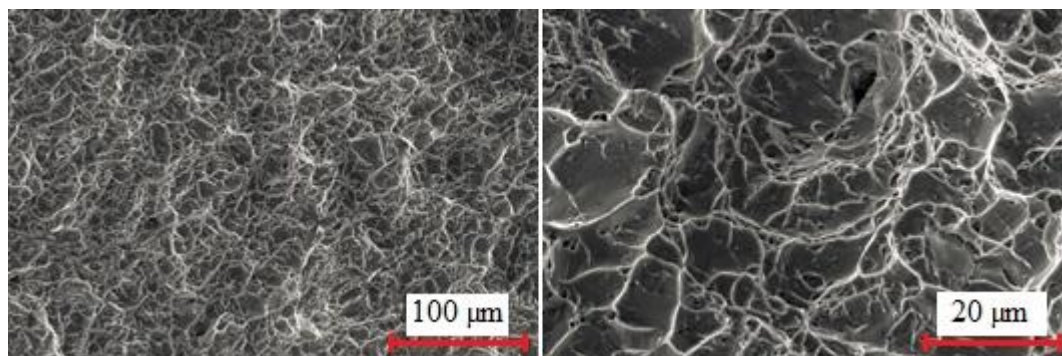


Figure 3.51 Fractography images of CR60 in 1000X (left) & 5000X (right).

As can be seen in Figure 3.51, the amount of dimples continued to decrease; conversely, the amount of quasi-cleavage surfaces continued to increase. Moreover, the surface is smoother than that of CR45. Figure 3.52 shows fractography images of CR75 in 1000X and 5000X magnification.

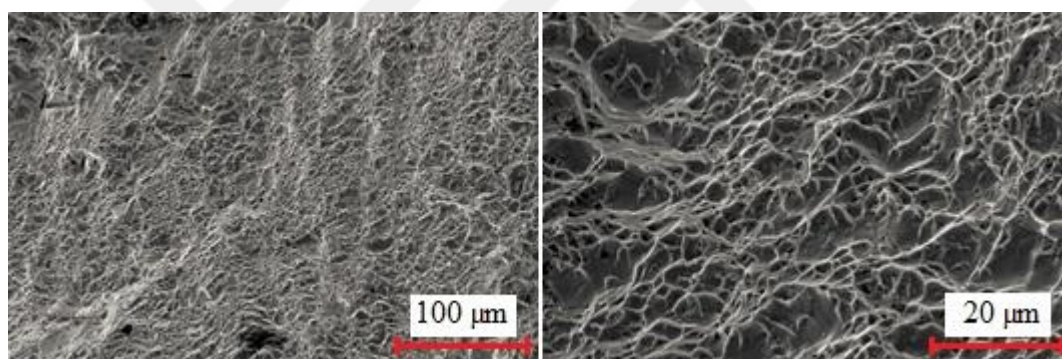


Figure 3.52 Fractography images of CR75 in 1000X (left) & 5000X (right).

As illustrated in Figure 3.52, the amount of quasi-cleavage surfaces reached to maximum in comparison with other samples. On the other hand, the amount of dimples is very little. Furthermore, the surface of CR75 is the smoothest one. As a result, AN is the most ductile, and CR75 is the most brittle sample. It can be concluded that the fracture behavior of samples altered from ductile to brittle with increasing of cold rolling reduction ratio.

CHAPTER 4

CONCLUSIONS AND FUTURE WORK

4.1 Conclusions

In this study, Zircaloy-4 rods are heat treated and cold rolled to different (15%, 30%, 45%, 60%, and 75%) reduction ratios to determine the effect of heat treatment and cold rolling on physical and mechanical properties.

Phase analysis, surface analysis, elemental analysis, fractography study, microstructural examination, and the investigation of mechanical properties are performed to illustrate the effects of heat treatment and cold working on Zircaloy-4 specimens.

Surface roughness tester measurement results showed that cold rolling reduced the surface roughness in microscale. Moreover, the surface is smoother after polishing and etching.

AFM measurement results illustrated that etching increased the surface roughness due to grain orientation. Furthermore, rolling directions of samples are smoother than transverse directions of samples in nanoscale.

Micro Vickers hardness tester measurement results showed that microhardness values of samples increased with increasing cold rolling reduction ratio in both rolling and transverse directions by grain refinement and work hardening mechanisms in microscale.

In addition, work hardening mechanism in rolling direction is more effective than that in transverse direction, and its effect increases with increasing reduction ratio. On the other hand, grain refinement mechanisms in both directions are similar. Furthermore, polishing and etching have very little reducing effect on microhardness values of samples in both rolling and transverse directions.

UMT measurement results illustrated that nanohardness and elastic modulus increased with increasing of cold rolling reduction ratio. Moreover, elastic modulus and hardness values of rolling direction of samples are higher than that of transverse direction of samples. Furthermore, load-depth figures of samples illustrate that the homogeneity of all samples are in a good level.

Microstructural analysis results showed that cold rolling has a positive effect on surface roughness. Moreover, the hardness increased with decreasing of grain size in rolling direction. In addition, average grain sizes of transverse directions are lower than average grain sizes of rolling directions.

Elemental analysis results showed that there are only alloying elements in structure, so rolling and annealing processes did not cause any contamination. Furthermore, a large quantity of oxygen is absorbed by each sample because of inappropriate storage conditions, high surface area due to rough surface derived from fracture, the quality problem of annealing furnace, and uncontrolled atmosphere and high temperature of heating steps of cold rolling process. On the other hand, oxygen absorption decreased with reduction of surface roughness due to increasing of cold rolling reduction ratio.

Phase analysis results illustrated that there is only Zr- α phase in structure. An oxide phase did not form due to dissolution of oxygen in interstitial positions of Zr- α structure.

Fractography study results showed that samples have mixed fracture mode with quasi-cleavage surfaces and dimples. Furthermore, the fracture behavior of samples altered from ductile to brittle with increasing of cold rolling reduction ratio.

4.2 Future Work

Zirconium alloys has a crucial role in nuclear reactor technology, so they should be investigated in all aspects. Fabrication processes like casting, rolling, and welding can be studied in a comprehensive manner. Mechanical properties of zirconium alloys can be investigated in detail by performing the tests under nuclear reactor conditions like high pressure, high temperature, and radiation.

Hydrogen embrittlement, oxygen absorption, and creep behavior of zirconium alloys are very important for safety of nuclear reactors. Therefore, these topics should be taken into consideration, and full-scale projects should be started in the near future.

Fabrication of new zirconium alloys should be studied to improve the mechanical and physical properties of zirconium cladding. Since the purchasing of nuclear grade zirconium from other countries is not feasible, zirconium purification techniques and separation of hafnium from zirconium can be investigated.

Degradation mechanisms, aging effect, and lifespan of nuclear reactors are important safety issues, so detailed research is needed for these topics.



REFERENCES

- [1] Mahaffey, J. A., “The History of Nuclear Power”, Facts on File, New York, 2011.
- [2] World Nuclear Power Reactors & Uranium Requirements. (n.d.). June 2, 2017, from [http:// www.world-nuclear.org/ information-library / facts-and-figures / world-nuclear-power-reactors-and-uranium-requireme.aspx](http://www.world-nuclear.org/information-library/facts-and-figures/world-nuclear-power-reactors-and-uranium-requireme.aspx)
- [3] Nero, A. V., “A Guidebook to Nuclear Reactors”, University of California Press, Berkeley, 1979.
- [4] Glasstone, S. & Sesonske, A., “Nuclear Reactor Engineering – Reactor Systems Engineering”(4th Ed., Vol. 2), Springer-Science+Business Media, Dordrecht, 1994.
- [5] Wood, J., “Nuclear Power”, The Institution of Engineering and Technology, London, 2007.
- [6] Hodge, B. K., “Alternative Energy Systems and Applications”(2nd Ed.), John Wiley & Sons Inc., New Jersey, 2017.
- [7] Filburn, T. & Bullard, S., “Three Mile Island, Chernobyl and Fukushima”, Springer International Publishing, Switzerland, 2016.
- [8] Zohuri, B. & McDaniel, P., “Thermodynamics in Nuclear Power Plant Systems”, Springer International Publishing, Switzerland, 2015.
- [9] Kessler, G., “Sustainable and Safe Nuclear Fission Energy”, Springer-Verlag, Heidelberg, 2012.
- [10] Duderstadt, J. J. & Hamilton, L. J., “Nuclear Reactor Analysis”, John Wiley & Sons Inc., New York, 1976.

- [11] Verfondern, K. & Nabielek, H. & Kania, M. J. & Allelein, H. J., “High-Quality Thorium TRISO Fuel Performance in HTGRs”, Forschungszentrum Jülich GmbH, Jülich, 2013.
- [12] Lewins, J., “Nuclear Reactor Kinetics and Control”, Pergamon Press, Oxford, 1978.
- [13] Oka, Y., “Nuclear Reactor Design”, Springer, Tokyo, 2014.
- [14] Hubbell, M. W., “The Fundamentals of Nuclear Power Generation”, AuthorHouse, Indiana, 2011.
- [15] Drbal, L. F. & Boston, P. G. & Westra, K. L. & Erickson, R. B., “Power Plant Engineering”, Kluwer Academic Publishers, Boston, 2003.
- [16] Jha, D. K., “Nuclear Energy”, Discovery Publishing House, New Delhi, 2004.
- [17] Ishikawa, M., “A Study of the Fukushima Daiichi Nuclear Accident Process”, Springer, Tokyo, 2015.
- [18] Cox, R. P. & Beyer, G. H., “Separation of Hafnium from Zirconium Using Tributyl Phosphate”, Ames Laboratory ISC Technical Reports, Washington, 1955.
- [19] Schweitzer, P. A., “Corrosion Engineering Handbook”, Marcel Dekker Inc., New York, 1996.
- [20] Mukherji, A. K., “Analytical Chemistry of Zirconium and Hafnium”, Pergamon Press, Oxford, 1970.
- [21] Schemel, J. H., “ASTM Manual on Zirconium and Hafnium”, ASTM, Florida, 1977.
- [22] Murray, G. T., “Handbook of Materials Selection for Engineering Applications”, Marcel Dekker Inc., New York, 1997.

- [23] Murty, K. L. & Charit, I., “An Introduction to Nuclear Materials”, Wiley-VCH Verlag, Weinheim, 2013.
- [24] Gharbi, N. & Onimus, F. & Gilbon, D. & Mardon, J. P. & Feaugas, X., “Impact of an Applied Stress on C-component Loops Under Zr Ion Irradiation in Recrystallized Zircaloy-4 and M5” *Journal of Nuclear Materials*, 467, 785-801, 2015.
- [25] Duan, Z. & Yang, H. & Satoh, Y. & Murakami, K. & Kano, S. & Zhao, Z. & Shen, J. & Abe, H., “Current Status of Materials Development of Nuclear Fuel Cladding Tubes for Light Water Reactors” *Nuclear Engineering and Design*, 316, 131-150, 2017.
- [26] Lu, K., “Materials in Energy Conversion, Harvesting, and Storage”, John Wiley & Sons Inc., New Jersey, 2014.
- [27] Yan, Y. & Burtseva, T. A. & Billone, M. C., “High-temperature Steam-oxidation Behavior of Zr-1Nb Cladding Alloy E110” *Journal of Nuclear Materials*, 393, 433-448, 2009.
- [28] Sehgal, B. R., “Nuclear Safety in Light Water Reactors”, Academic Press, Massachusetts, 2012.
- [29] Kim, H. H. & Kim, J. H. & Moon, J. Y. & Lee, H. S. & Kim, J. J. & Chai, Y. S., “High-temperature Oxidation Behavior of Zircaloy-4 and Zirlo in Steam Ambient” *Journal of Materials Science & Technology*, 26(9), 827-832, 2010.
- [30] Seok, C. S. & Marple, B. & Song, Y. J. & Gollapudi, S. & Charit, I. & Murty, K. L., “High Temperature Deformation Characteristics of Zirlo™ Tubing via Ring-creep and Burst Tests” *Nuclear Engineering and Design*, 241, 599-602, 2011.
- [31] Koutsky, J. & Kocik, J., “Radiation Damage of Structural Materials”, Elsevier Science Publishers, Czech Republic, 1994.

- [32] Nemoto, Y. & Kaji, Y. & Ogawa, C. & Kondo, K. & Nakashima, K. & Kanazawa, T. & Tojo, M., "Investigation of Zircaloy-2 Oxidation Model for SFP Accident Analysis" *Journal of Nuclear Materials*, 488, 22-32, 2017.
- [33] Waheed, A. F. & Kandil, A. T. & Hamed, H. M., "Electrochemical corrosion of Zircaloy-2 under PWR Water Chemistry but at Room Temperature" *Annals of Nuclear Energy*, 94, 168-174, 2016.
- [34] Goel, S. & Jayaganthan, R. & Singh, I. V. & Srivastava, D. & Dey, G. K. & Saibaba, N., "Mechanical and Microstructural Characterizations of Ultrafine Grained Zircaloy-2 Produced by Room Temperature Rolling" *Materials and Design*, 55, 612-618, 2014.
- [35] Whitmarsh, C. L., "Review of Zircaloy-2 and Zircaloy-4 Properties Relevant to N. S. Savannah Reactor Design", Oak Ridge National Laboratory, Tennessee, 1962.
- [36] Cockeram, B. V. & Chan, K. S., "In situ Studies and Modeling the Fracture of Zircaloy-4" *Journal of Nuclear Materials*, 393, 387-408, 2009.
- [37] Baek, J. H. & Jeong, Y. H., "Depletion of Fe and Cr within Precipitates During Zircaloy-4 Oxidation" *Journal of Nuclear Materials*, 304, 107-116, 2002.
- [38] Darrieulat, M. & Ammar, Y. B. & Aoufi, A., "Processing of β -treated Zircaloy-4 by Warm Compressions Along Three Orthogonal Axes" *Journal of Materials Science*, 50, 2709-2725, 2015.
- [39] Suman, S. & Khan, M. K. & Pathak, M. & Singh, R. N., "Effects of Hydride on Crack Propagation in Zircaloy-4" *Procedia Engineering*, 173, 1185-1190, 2017.
- [40] Yoo, J. S. & Kim, I. S., "Texture Transformations and Its Role on the Yield Strength of (α + β) Heat Treated Zircaloy-4" *Journal of the Korean Nuclear Society*, 24(1), 75-85, 1992.

- [41] Dupim, I. S. & Moreira, J. M. L. & Huot, J. & Santos, S. F., “Effect of Cold Rolling on the Hydrogen Absorption and Desorption Kinetics of Zircaloy-4” *Materials Chemistry and Physics*, 155, 241-245, 2015.
- [42] Fuloria, D. & Kumar, N. & Goel, S. & Jayaganthan, R. & Jha, S. & Srivastava, D., “Tensile Properties and Microstructural Evolution of Zircaloy-4 Processed Through Rolling at Different Temperatures” *Materials and Design*, 103, 40-51, 2016.
- [43] Cockeram, B. V. & Hollenbeck, J. L., “The Role of Stress-state on the Deformation and Fracture Mechanism of Hydrided and Non-hydrided Zircaloy-4” *Journal of Nuclear Materials*, 467, 9-31, 2015.
- [44] Steinbrück, M. & Birchley, J. & Boldyrev, A. V. & Goryachev, A. V. & Grosse, M. & Haste, T. J. & Hozer, Z. & Kisselev, A. E. & Nalivaev, V. I. & Semishkin, V. P. & Sepold, L. & Stuckert, J. & Ver, N. & Veshchunov, M. S., “High-temperature Oxidation and Quench Behaviour of Zircaloy-4 and E110 Cladding Alloys” *Progress in Nuclear Energy*, 52, 19-36, 2010.
- [45] Lim, Y. S. & Kim, H. G. & Jeong, Y. H., “Experimental Evolution of the Rolling Reduction and Heat-treatment Effects on the Texture and Creep Behavior of a Zircaloy-4 Sheet” *Materials Transactions*, 49(8), 1922-1925, 2008.
- [46] Gloaguen, D. & Fajoui, J. & Girault, B., “Residual Stress Fields Analysis in Rolled Zircaloy-4 Plates: Grazing Incidence Diffraction and Elastoplastic Self-Consistent Model” *Acta Materialia*, 71, 136-144, 2014.
- [47] Busser, V. & Dubourg, M. C. B. & Desquines, J. & Duriez, C. & Mardon, J. P., “Mechanical Response of Oxidized Zircaloy-4 Cladding Material Submitted to a Ring Compression Test” *Journal of Nuclear Materials*, 384, 87-95, 2009.
- [48] Samal, M. K. & Sanyal, G. & Chakravartty, J. K., “Investigation of Failure Behavior of Two Different Types of Zircaloy Clad Tubes Used as Nuclear Fuel Rod Pins” *Engineering Failure Analysis*, 18, 2042-2053, 2011.

- [49] Berger, P. & El Tahhann, R. & Moulin, G. & Viennot, M., “High Temperature Oxidation of Zirconium and Zircaloy-4 Under Applied Load: Nuclear Microprobe Study of the Growth of the Oxide” *Nuclear Instruments and Methods in Physics Research B*, 210, 519-525, 2003.
- [50] De Menibus, A. H. & Auzoux, Q. & Mongabure, P. & Macdonald, V. & Le Jolu, T. & Besson, J. & Crepin, J., “Fracture of Zircaloy-4 Cladding Tubes With or Without Hydride Blisters in Uniaxial to Plane Strain Conditions With Standard and Optimized Expansion due to Compression Tests” *Materials Science & Engineering A*, 604, 57-66, 2014.
- [51] Cockeram, B. V. & Chan, K. S., “In Situ Studies and Modeling of the Deformation and Fracture Mechanism for Wrought Zircaloy-4 and Zircaloy-2 as a Function of Stress-state” *Journal of Nuclear Materials*, 434, 97-123, 2013.
- [52] Tong, V. S. & Britton, T. B., “Formation of Very Large ‘Blocky Alpha’ Grains in Zircaloy-4” *Acta Materialia*, 129, 510-520, 2017.
- [53] Kim, J. H. & Lee, M. H. & Choi, B. K. & Jeong, Y. H., “Failure Behavior of Zircaloy-4 Cladding After Oxidation and Water Quench” *Journal of Nuclear Materials*, 362, 36-45, 2007.
- [54] Jung, S. H. & Kim, I. S., “Effect of β -Heat Treatment on Microstructure and Mechanical Anisotropy of Zircaloy-4 Fuel Cladding” *Journal of Nuclear Science and Technology*, 26(5), 516-524, 1989.
- [55] Coindreau, O. & Duriez, C. & Ederli, S., “Air Oxidation of Zircaloy-4 in the 600-1000°C Temperature Range: Modeling for ASTEC Code Application” *Journal of Nuclear Materials*, 405, 207-215, 2010.
- [56] Matsunaga, T. & Satoh, Y. & Abe, H., “Accumulation of Plastic Strain in Zircaloy-4 at Low Homologous Temperature” *Journal of Nuclear Materials*, 465, 358-363, 2015.

- [57] Sakharova, N. A. & Fernandes, J. V. & Antunes, J. M. & Oliveira, M. C., “Comparison Between Berkovich, Vickers, and Conical Indentation Tests: A Three-dimensional Numerical Simulation Study” *International Journal of Solids and Structures*, 46, 1095-1104, 2009.
- [58] Whitehouse, D. J., “Handbook of Surface and Nanometrology”(2nd Ed.), CRC Press, Boca Raton, 2011.
- [59] Totten, G. E. & Funatani, K. & Xie, L., “Handbook of Metallurgical Process Design”, Marcel Dekker Inc., New York, 2004.
- [60] Baboian, R., “Corrosion Tests and Standards: Application and Interpretation”(2nd Ed.), ASTM International, Philadelphia, 2005.
- [61] Fischer, X. & Daidie, A. & Eynard, B. & Paredes, M., “Research in Interactive Design Vol. 4: Mechanics, Design Engineering and Advanced Manufacturing”, Springer International Publishing, Switzerland, 2016.
- [62] Yılmaz, F., “Farklı Yöntemlerle Üretilen AB₅ Tipi Hidrojen Depolayan Alaşımların Karakterizasyonu”, Ph.D. Thesis, Gaziosmanpaşa University, Graduate School of Natural and Applied Sciences, Tokat-Turkey, 2014.
- [63] Yılmaz, F., “Nanokristal Al-Si-Sb Alaşımlarının Enerji Yaklaşımı ile Mikromekanik Karakterizasyonu”, M.Sc. Thesis, Gaziosmanpaşa University, Graduate School of Natural and Applied Sciences, Tokat-Turkey, 2008.
- [64] Trivedi, P. & Patel, A. K. & Maurya, R. & Jayaganthan, R. & Balani, K., “Nanomechanical Characterization and Protein Adsorption of Cold-Rolled Zirconium Alloy” *The Minerals, Metals & Materials Society*, 67(4), 726-732, 2015.
- [65] Ito, M. & Muta, H. & Setoyama, D. & Uno, M. & Yamanaka, S., “Nanoindentation Studies of High-temperature Oxidized Zircaloy-4 with and without Hydrogen” *Journal of Alloys and Compounds*, 446-447, 639-642, 2007.

- [66] De Menibus, A. H. & Auzoux, Q. & Dieye, O. & Berger, P. & Bosonnet, S. & Foy, E. & Macdonald, V. & Besson, J. & Crepin, J., “Formation and Characterization of Hydride Blisters in Zircaloy-4 Cladding Tubes” *Journal of Nuclear Materials*, 449, 132-147, 2014.
- [67] Akhiani, H. & Szpunar, J. A., “Effect of Surface Roughness on the Texture and Oxidation Behavior of Zircaloy-4 Cladding Tube” *Applied Surface Science*, 285P, 832-839, 2013.
- [68] Platt, P. & Allen, V. & Fenwick, M. & Gass, M. & Preuss, M., “Observation of the Effect of Surface Roughness on the Oxidation of Zircaloy-4” *Corrosion Science*, 98, 1-5, 2015.
- [69] Daub, K. & Nieuwenhove, R. V. & Nordin, H., “Investigation of the Impact of Coatings on Corrosion and Hydrogen Uptake of Zircaloy-4” *Journal of Nuclear Materials*, 467, 260-270, 2015.
- [70] Lichter, B. D., “Precision Lattice Parameter Determination of Zirconium Oxygen Solid Solution” *Phase Transitions*, 38, 127-220, 1992.
- [71] Selmi, N. & Sari, A., “Study of Oxidation Kinetics in Air of Zircaloy-4 by In-situ X-Ray Diffraction” *Advances in Materials Physics and Chemistry*, 3, 168-173, 2013.
- [72] Callister, W. D. & Rethwisch, D. G., “Materials Science and Engineering, SI Version”(8th Ed.), John Wiley & Sons Inc., New York, 2011.
- [73] Wulpi, D. J., “Understanding How Components Fail”(3th Ed.), ASM International, Ohio, 2013.

CURRICULUM VITAE

PERSONAL INFORMATION

Name Surname : Semih AĞCA
Date of Birth : 1986
Phone : +90 555 4765586
E-mail : sagca@ybu.edu.tr



EDUCATION

High School : Karatay Anatolian High School / KONYA (2000-2004)
(4.01/5)
Bachelor : Gazi University / ANKARA (2006-2010)
(3.53/4.0)
Master Degree : Gazi University / ANKARA (2012-2016)
(3.71/4.0)
Master Degree : Ankara Yıldırım Beyazıt University / (2014-continued)

WORK EXPERIENCE

Research Assist. : Gazi University / (2011-2014)
Research Assist. : Ankara Yıldırım Beyazıt University / (2014-continued)

TOPICS OF INTEREST

- Zirconium Alloys
- Functionally Graded Materials
- Centrifugal Casting
- Smart Materials